

A new timescale-mass scaling for the optical variation of active galactic nuclei across the intermediate-mass to supermassive scales

ZHEN-BO SU ^{1,2} ZHEN-YI CAI ^{1,2} MOUYUAN SUN ³ HENGXIAO GUO ⁴ WEI-MIN GU ³ AND JUN-XIAN WANG ^{1,2}

¹CAS Key Laboratory for Research in Galaxies and Cosmology, Department of Astronomy, University of Science and Technology of China, Hefei 230026, China

²School of Astronomy and Space Science, University of Science and Technology of China, Hefei 230026, China

³Department of Astronomy, Xiamen University, Xiamen 361005, China

⁴Shanghai Astronomical Observatory, Chinese Academy of Sciences, 80 Nandan Road, Shanghai 200030, China

(Revised May 7, 2024)

ABSTRACT

Variability of active galactic nuclei (AGNs) has long been servicing as an essential avenue of exploring the accretion physics of black hole (BH). There are two commonly used methods for analyzing AGN variability. First, the AGN variability, characterized by the structure function (SF) of a single band, can be well described by a damped random walk (DRW) process on timescales longer than \sim weeks, shorter than which departures have been reported. Second, the color variation (CV) between two bands behaves timescale-dependent, raising challenges to the widely accepted reprocessing scenario. However, both the departure from the DRW process and the timescale-dependent CV are hitherto limited to AGNs, mainly quasars, at the supermassive scale. Here, utilizing the high-cadence multi-wavelength monitoring on NGC 4395 harboring an intermediate-mass BH, we unveil at the intermediate-mass scale for the first time, prominent departures from the DRW process at timescales shorter than \sim hours in all three nights and bands, and plausible timescale-dependent CVs in the two longest nights of observation. Furthermore, comparing SFs of NGC 4395 to four AGNs at the supermassive scale, we suggest a new scaling relation between the timescale (τ ; across nearly three orders of magnitude) and the BH mass (M_{BH}): $\tau \propto M_{\text{BH}}^\gamma$ where the exponent γ is likely $\simeq 0.6 - 0.8$. This exponent differs from most previous measurements, but confirms a few and is consistent with a recent theoretical prediction, suggesting a similar accretion process in AGNs across different mass scales.

Keywords: Active galactic nuclei; Time domain astronomy

1. INTRODUCTION

The ultraviolet-to-optical (UV/optical) continuum emission of active galactic nuclei (AGNs), which encompass luminous quasars and their low-luminosity counterparts, is believed to originate from the accretion disk surrounding the central massive black hole (BH). Since the angular sizes of the majority of AGNs are too small to be spatially resolved by the current best telescopes, studying AGN variability in UV/optical provides an al-

ternative avenue of unveiling the physics of the AGN central engine.

Hitherto, many properties of AGN variability have been found. In the UV/optical, the stochastic AGN variability can be well characterized by a damped random walk (DRW) process as least on timescales of weeks to years (e.g., Kelly et al. 2009; Zu et al. 2013a; Kozłowski 2016). Then correlations between the DRW parameters (i.e., the de-correlation or damping timescale, τ_d , and the asymptotic variability amplitude on long timescales, SF_∞) and the physical properties of AGNs, such as the BH mass, the Eddington ratio, and the luminosity, have been explored (e.g., Kelly et al. 2009; Kozłowski et al. 2010; MacLeod et al. 2010; Caplar et al. 2017;

Sun et al. 2018; Suberlak et al. 2021; Burke et al. 2021; Tang et al. 2023; Arévalo et al. 2023a). However, departures from the DRW process have been reported at timescales shorter than \sim weeks (e.g., Mushotzky et al. 2011; Kelly et al. 2014; Kasliwal et al. 2015; Simm et al. 2016), probably at timescales longer than years (Guo et al. 2017), and at shorter extreme UV wavelengths (Zhu et al. 2016). Note that these known departures from the DRW process are only found in quasars and AGNs with typically BHs massive than $\sim 10^7 M_{\odot}$.

In addition, by analyzing variations between UV/optical continuum bands, the variation at shorter wavelength (bluer band) is usually larger than that at longer wavelength (redder band), which is widely known as the bluer-when-brighter (BWB) color variation (CV) since Cutri et al. (1985; see also, e.g., Schmidt et al. 2012; Zuo et al. 2012; Ruan et al. 2014; Guo & Gu 2016). Understanding on the CV had not been refurbished until Sun et al. (2014) who discovered that the ensemble CV of the Sloan Digital Sky Survey (SDSS) Stripe 82 quasars is timescale-dependent, that is, the CV is more prominent at shorter timescales. The timescale-dependent CV immediately demonstrates that the origin of the CV is neither attributed to a simple combination of a variable AGN with a fixed bluer spectral slope and an invariable redder host galaxy (Sun et al. 2014), nor to changes in the global accretion rates (Cai et al. 2016). Instead, it suggests that the CV is intrinsic to the accretion disk, and furthermore supports an origin of the thermal fluctuation for the UV/optical variation in quasars (Cai et al. 2016; see also Kelly et al. 2009; Dexter & Agol 2011).

The power of analyzing the timescale-dependent CV is striking. By extending the color analysis on a quasar sample observed at shorter rest-frame wavelengths from near UV to extreme UV, Zhu et al. (2016) not only confirmed the timescale dependence in the UV but also unveiled that the thermal fluctuation in the inner disk may deviate from the DRW process. Moreover, comparing the CV difference between the radio-loud and radio-quiet quasars, Cai et al. (2019) suggested that the inner disks in the radio-loud quasars may be more stable, providing new clues to the jet launching. From quasar samples to individual AGNs, the role of analyzing the timescale-dependent CV is also attractive. Zhu et al. (2018) successfully identified for the first time the UV/optical timescale-dependent CV in an individual AGN, i.e., NGC 5548 (at $z = 0.017175$ and with $M_{\text{BH}} \sim 5 \times 10^7 M_{\odot}$; Pancoast et al. 2014), challenging the traditional thermal reprocessing scenario, where the UV/optical variation is assumed to be the thermal reprocessing of the variable X-ray emission. In another in-

dividual AGN, i.e., NGC 4051 (with $M_{\text{BH}} \sim 2 \times 10^6 M_{\odot}$; Denney et al. 2009), Wu et al. (2020) found that the timescale-dependent CV between two hard X-ray bands hints at random individual solar-like flares perturbing the global variation of the extended corona.

Unfortunately, the timescale-dependent CV has not gotten enough attention by the community even we have progressively developed the method and have applied it to more and more situations aforementioned over the past decade. Furthermore, the timescale-dependent CV, as well as the aforementioned departure from the DRW process, are hitherto found in quasars or AGNs whose BH masses are larger than $10^{6-7} M_{\odot}$.

Recently, exploring the optical variation properties of AGNs (Burke et al. 2020; Montano et al. 2022; McHardy et al. 2023) has been extended to a nearby dwarf galaxy, NGC 4395 (at a redshift of $z = 0.001064$; Filippenko & Sargent 1989; den Brok et al. 2015), harboring an intermediate-massive BH (IMBH) with a BH mass of $\sim 10^{4-5} M_{\odot}$ (e.g., Filippenko & Ho 2003; Peterson et al. 2005; Woo et al. 2019; Cho et al. 2021). On one hand, using \sim month-long and 30 minute-cadence observations of the Transiting Exoplanet Survey Satellite (TESS), Burke et al. (2020) found that the optical variation of NGC 4395 can also be described by the same DRW process as the luminous quasars. On the other hand, both Montano et al. (2022) and McHardy et al. (2023) mainly focus on the inter-band lags.

Here, benefiting from these recent very high cadence (as short as several seconds to several minutes) and simultaneous multi-band monitoring campaigns (Montano et al. 2022; McHardy et al. 2023), we revisit the optical variation properties of NGC 4395 and unveil at the intermediate-mass scale for the first time a prominent departure from the DRW process and a plausible timescale-dependent CV. Section 2 successively introduces the multi-band light curves of NGC 4395, the structure functions (SFs), and the CVs, complemented with the methodology for automatically determining a proper range of time intervals where results on the SF or CV are not significantly affected by either the photometric uncertainty at short timescales or the limited length of the light curve at long timescales. Discussions are presented in Section 3, followed by a brief summary in Section 4.

The codes used in this work are available on Zenodo: [doi:10.5281/zenodo.10428783](https://doi.org/10.5281/zenodo.10428783).

2. OPTICAL VARIATION PROPERTIES OF NGC 4395

2.1. Light Curves

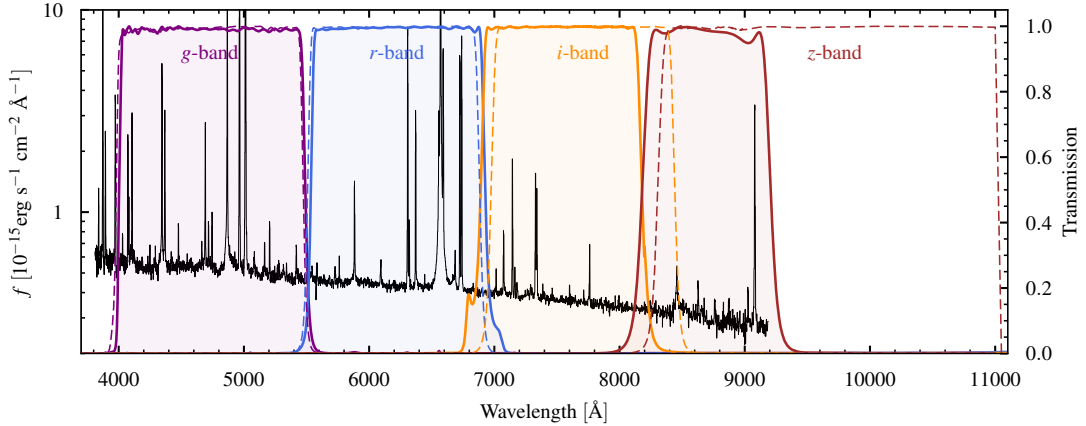


Figure 1. The FNT (colored solid curves with shaded regions) and GTC (colored dashed curves) *griz*-band transmission curves (right *y*-axis) on top of an SDSS spectrum for NGC 4395 (black; left *y*-axis).

Using a four-channel MuSCAT3 camera on the 2 m Faulkes North Telescope (FNT) simultaneously observing in g' , r' , i' , and z'_s bands¹, Montano et al. (2022) monitored NGC 4395 in two consecutive nights: ~ 6.7 hr on 2022 April 26 (hereafter, the FNT-1) and ~ 6.2 hr on 2022 April 27 (hereafter, the FNT-2). The typical cadences in the g' , i' , and z'_s bands are 103.68 s, while denser cadences of 34.56 s are found in the r' band. Since analyzing the CV requires quasi-simultaneous observations and instants among these four bands are not exactly the same, we re-bin all four light curves in the same bin sizes of 103.68 s. Within a bin, multiple flux points, found primarily in the r' band, are averaged and the associated errors are propagated accordingly.

Similarly, NGC 4395 was simultaneously observed in u_s , g_s , r_s , i_s , and z_s bands² by McHardy et al. (2023) for 6 hr from 2018 April 16 to 17 with HiPERCAM on the 10.4 m Gran Telescopio Canarias (GTC). The cadences are as short as 3 s for the g_s , r_s , i_s , and z_s bands, and 15 s for the u_s band. In order to compare the variation properties between McHardy et al. (2023) and Montano et al. (2022), we exclude the u_s band. Moreover, we only consider the light curves within the first 8000 s as strongly suggested by McHardy et al. (2023, affected by the loss of tracking as a result of the motion of NGC 4395 and the calibration stars over the CCDs). The AGN magnitudes have been derived combining the count-rate

ratios of the AGN to Star 1 with the SDSS magnitudes of star 1 (cf. Table 2 of McHardy et al. 2023). Note that the flux calibration may not be particularly accurate since Star 1 might have varied slightly since measured by SDSS (I. McHardy 2023, private communication).

Figure 1 displays the FNT and GTC transmission curves on top of an SDSS spectrum (MJD = 53819, PlateID = 2015, and FiberID = 251) for NGC 4395. Since the filter differences are small (except the z'_s/z_s band), we simply use the same abbreviation *griz* hereafter. Figure 2 illustrates the *griz*-band light curves of NGC 4395 in three nights used in this work, whose flux densities are in units of $\text{erg s}^{-1} \text{cm}^{-2} \text{\AA}^{-1}$. Note that differences in the mean flux densities between Montano et al. (2022) and McHardy et al. (2023) are not large, i.e., $\lesssim 17\%$. Table 1 tabulates the mean flux density, the mean photometric uncertainty (σ_e), and the variation amplitude for each band and night. Following Vaughan et al. (2003), the variation amplitude in each band is characterized by the excess variation, σ_{rms} . Figure 3 illustrates σ_{rms} as well as the significance of variation, $\sigma_{\text{rms}}/\sigma_e$, as a function of wavelength.

2.2. Structure Functions

The SF of a single-band light curve measures the typical variation amplitude as a function of time intervals (hereafter timescales). Generally, given an observed light curve, the observed SF can be derived by (e.g., di Clemente et al. 1996; Kozłowski 2016)

$$\text{SF}_{\text{obs}}(\tau) = \sqrt{\frac{\pi}{2} \langle |m_i - m_j|^2 \rangle} \quad \text{mag}, \quad (1)$$

where m_i and m_j are magnitudes at t_i and t_j instants, respectively, and the time interval between two instants

¹ The central wavelengths of the g' , r' , i' , and z'_s bands are 4770 Å, 6215 Å, 7545 Å, and 8700 Å, respectively (Montano et al. 2022, cf. their Table 2). See <https://lco.global/observatory/instruments/filters> for filters and Figure 1 for an illustration.

² The effective wavelengths of the g_s , r_s , i_s , and z_s bands are 4778 Å, 6201 Å, 7640 Å, and 9066 Å, respectively (McHardy et al. 2023, cf. their Table 3). See <http://www.vikdhillon.staff.shef.ac.uk/ultracam/filters/filters.html> for filters and Figure 1 for an illustration.

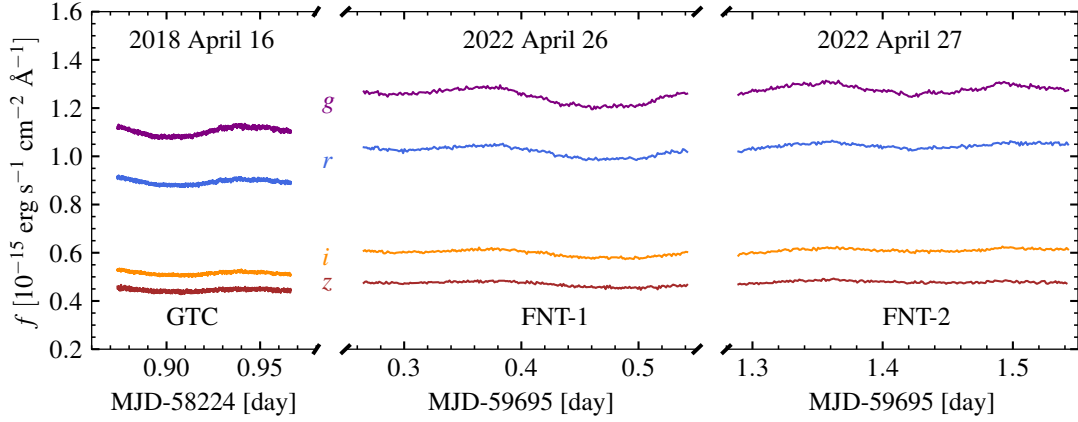


Figure 2. Recent very high cadence and multi-band (g , r , i , and z from top to bottom, respectively) light curves of NGC 4395 observed in three nights on 2018 April 16 (2.2 hr; McHardy et al. 2023) and on 2022 April 26 to 27 (6.7 hr and 6.2 hr; Montano et al. 2022). The g -, r -, i -, and z -band mean fluxes of McHardy et al. (2023) are slightly smaller than those of Montano et al. (2022, average over two nights) by factors of $\simeq 1.15$, $\simeq 1.15$, $\simeq 1.17$, and $\simeq 1.07$, respectively (Table 1). The flux densities are in units of $10^{-15} \text{ erg s}^{-1} \text{ cm}^{-2} \text{ \AA}^{-1}$.

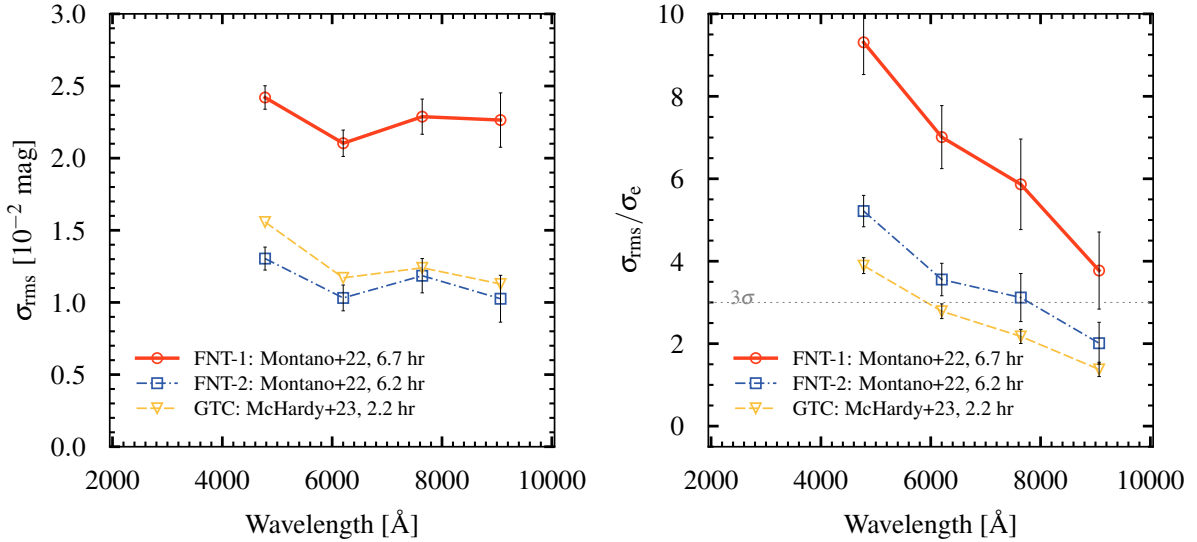


Figure 3. Left panel: the excess variance, σ_{rms} , as a function of wavelength for NGC 4395 monitored in three nights (Table 1): FNT-1 (open circles), FNT-2 (open squares), and GTC (open triangles). Right panel: the significance of variation, $\sigma_{\text{rms}}/\sigma_e$, as a function of wavelength, where σ_e is the mean photometric uncertainties in magnitude (Table 1). The dotted horizontal line indicates a 3σ level.

$\tau = |t_i - t_j|$. At short timescales, the observed SF is dominated by the photometric uncertainties, σ_n . Following the suggestion of Kozłowski (2016), the underlying true SF, SF_{true} , could be inferred through

$$\text{SF}_{\text{obs}}^2(\tau) = \text{SF}_{\text{true}}^2(\tau|\tau_d, \beta, \text{SF}_{\infty}) + 2\sigma_n^2 \quad (2)$$

once a specific functional form for the true SF has been assumed. For instance,

$$\text{SF}_{\text{true}}(\tau|\tau_d, \beta, \text{SF}_{\infty}) = \text{SF}_{\infty} \sqrt{1 - \exp\left(-\frac{\tau}{\tau_d}\right)^\beta}, \quad (3)$$

where τ_d is the de-correlation or damping timescale, SF_{∞} is the asymptotic rms variability on long timescales, and β is the SF slope at $\tau \ll \tau_d$. Note that when $\tau \rightarrow 0$, $\text{SF}_{\text{obs}} \rightarrow \sqrt{2}\sigma_n$. On short timescales, i.e., $\ll \tau_d$, the power-law slopes of the SF and PSD are 0.5β and -2β , respectively. Since Kelly et al. (2009), many works suggest that the DRW process with $\beta = 1$ can well describe the stochastic behavior of the optical AGN variability, in particular for quasars/AGNs with SMBHs over timescales of several weeks to years (e.g., Kozłowski

Table 1. Variation properties of NGC 4395 and the best-fit parameters for its SFs.

Date	Band	\bar{f}^x	σ_{rms}	σ_e^x	σ_n	β	τ_d	SF $_{\infty}$
			(10^{-2} mag)	(10^{-2} mag)	(10^{-2} mag)		(10^3 s)	(10^{-2} mag)
(1)	(2)	(3)	(4)	(5)	(6)	(7)	(8)	(9)
2018 April 16 GTC	<i>g</i>	1.10	1.56 ± 0.07	0.40 ± 0.01	0.38 ± 0.01	1.79 ± 0.02	2.5 ± 0.1	3.7 ± 0.1
	<i>r</i>	0.89	1.17 ± 0.07	0.42 ± 0.01	0.39 ± 0.01	1.84 ± 0.03	2.2 ± 0.1	2.8 ± 0.1
	<i>i</i>	0.52	1.24 ± 0.10	0.57 ± 0.01	0.54 ± 0.01	1.75 ± 0.04	2.1 ± 0.1	3.0 ± 0.1
	<i>z</i>	0.44	1.13 ± 0.14	0.82 ± 0.03	0.86 ± 0.01	1.69 ± 0.09	2.3 ± 0.3	2.6 ± 0.2
2022 April 26 FNT-1	<i>g</i>	1.25	2.42 ± 0.08	0.26 ± 0.02	0.36 ± 0.02	1.88 ± 0.07	6.7 ± 0.4	5.2 ± 0.2
	<i>r</i>	1.02	2.10 ± 0.09	0.30 ± 0.03	0.38 ± 0.02	1.80 ± 0.08	7.8 ± 0.7	4.7 ± 0.2
	<i>i</i>	0.60	2.29 ± 0.12	0.39 ± 0.07	0.52 ± 0.03	1.68 ± 0.08	9.2 ± 1.0	5.3 ± 0.2
	<i>z</i>	0.47	2.26 ± 0.19	0.60 ± 0.14	0.69 ± 0.03	1.80 ± 0.12	12.6 ± 2.4	6.2 ± 0.7
2022 April 27 FNT-2	<i>g</i>	1.28	1.30 ± 0.08	0.25 ± 0.01	0.36 ± 0.03	1.73 ± 0.13	3.8 ± 0.6	2.9 ± 0.3
	<i>r</i>	1.04	1.03 ± 0.09	0.29 ± 0.02	0.38 ± 0.02	1.76 ± 0.20	5.0 ± 1.4	2.4 ± 0.4
	<i>i</i>	0.61	1.19 ± 0.12	0.38 ± 0.06	0.52 ± 0.03	1.87 ± 0.25	3.5 ± 0.6	2.2 ± 0.2
	<i>z</i>	0.47	1.03 ± 0.16	0.51 ± 0.10	0.63 ± 0.04	1.96 ± 0.45	3.0 ± 0.6	1.7 ± 0.2

NOTE— Column (1): the dates when NGC 4395 was observed by GTC on 2018 April 16 (McHardy et al. 2023) and by FNT on 2022 April 26 and 27 (Montano et al. 2022). Column (2): the name of the observed band. Column (3): \bar{f}^x is the x -band mean flux density, where x takes g , r , i , or z , in units of 10^{-15} erg s $^{-1}$ cm $^{-2}$ Å $^{-1}$. Column (4): σ_{rms} is the excess variance, calculated using Equation (8) of Vaughan et al. (2003), whose error is obtained using their Equation (11). Column (5): the mean and 1σ standard deviation of the x -band photometric uncertainties in magnitude, σ_e^x , converted from the initial flux densities and the associated errors. Columns (6) to (9): the best-fit parameters of σ_n , β , τ_d , and SF $_{\infty}$ in Equation (2) as well as the corresponding 1σ uncertainties.

et al. 2010; MacLeod et al. 2010; Andrae et al. 2013; Zu et al. 2013b).

The left panel of Figure 4 illustrates the observed i -band SFs for NGC 4395 in three nights. Here, the observed SFs are measured between 1 s and 10^5 s in steps of 0.05 dex, and the 1σ uncertainties are estimated via the standard deviations of SFs derived from 10^3 mock light curves, which are generated using the flux randomization/random subset selection method (e.g., Fausnaugh et al. 2016). On timescales shorter than $\sim 10^{2-3}$ s, the observed SFs are flat because of the photometric uncertainties; on timescales longer than $\sim 10^4$ s, the observed SFs show large statistical fluctuation due to the limited baseline of the observed light curve. The SFs of NGC 4395 varies between the three nights of observation, partly attributed to the randomness nature of AGN variability.

Throughout this work we should present all results based on every night of observation on NGC 4395. However, we suggest that the results based on the FNT-1 light curves may be the most reliable. On one hand, the FNT-1 light curves are the longest among the three nights available (Figure 2). The FNT-1/2 light curves are longer by a factor of $\simeq 3$ than the GTC light curves.

Although the FNT-1 light curves are merely longer by $\simeq 7.5\%$ than the FNT-2 light curves, the resultant FNT-1 SFs flatten at $\simeq 1.3 \times 10^4$ s, which is nearly $\simeq 2$ times the turnover timescale of the FNT-2 SFs (see the left panel of Figure 4 and the best-fit τ_d in Table 1). On the other hand, as demonstrated in Figure 3, both the variation amplitude (σ_{rms}) and the significance of the variation ($\sigma_{\text{rms}}/\sigma_e$) of the FNT-1 light curves are larger by a factor of $\simeq 2$ than those of the FNT-2 and GTC light curves. Nevertheless, we would end up with our current conclusions considering also the results based on the FNT-2 light curves, which have comparable baseline to the FNT-1 light curves, and leaving firm conclusions for future more and better data on NGC 4395.

2.2.1. A Proper Range of Timescales for the SF

Since the observed SFs at timescales longer than $\sim 10^4$ s are subject to substantial statistical fluctuations, we follow Emmanoulopoulos et al. (2010) and take a specific timescale, τ_{max} , at the first local maximum of the observed SF as the right borderline for the proper range of timescales of the SF. In the left panel of Figure 4 the observed SFs beyond τ_{max} shown in the light-gray are not used in the following. To determine a minimal timescale, τ_{min} , as the left borderline for the proper

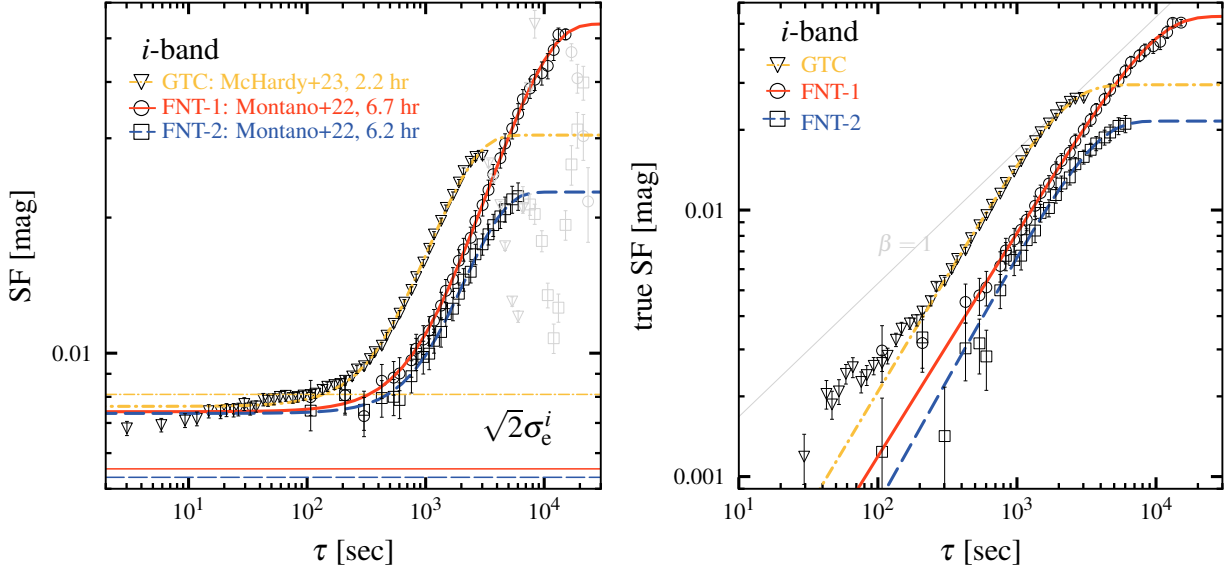


Figure 4. Left panel: The observed *i*-band FNT-1 (open circles), FNT-2 (open squares), and GTC (open triangles) SFs of NGC 4395 are fit by Equation (2) after excluding a few uncertain data points (light-gray) at long timescales (i.e., $\tau > \tau_{\max}$; see Section 2.2). Including the best-fit photometric uncertainties, σ_n (i.e., the horizontal part of the observed SFs at $\tau \lesssim 10^{2-3}$ s; see Table 1), the best-fit FNT-1 (thick solid curve), FNT-2 (thick dashed curve), and GTC (thick dot-dashed curve) SFs are shown. For comparison, the reported *i*-band mean photometric uncertainties, σ_e^i , for the three datasets are shown in the same style but with thinner horizontal lines. Comparing the reported σ_e^i to the best-fit σ_n , McHardy et al. (2023) may slightly overestimate the photometric uncertainties by a factor of $\simeq 1.1$, while Montano et al. (2022) may underestimate them by a factor of $\simeq 1.4$. Therefore, the best-fit σ_n is used to determine the left borderline for the proper range of timescales of the SF (see Section 2.2.1). Right panel: after subtracting the best-fit σ_n (Equation 2) and excluding unfit data points at $\tau > \tau_{\max}$, the corresponding true SFs (symbols) and best-fit (curves) SFs are compared. The true SFs inferred from three nights have similar short-term slopes, $\beta \simeq 1.8$, regardless of the large differences in both τ_d and SF_∞ (Table 1). Departures from the DRW process with $\beta = 1$ (the light-gray thin solid line) are prominent at timescales shorter than \sim hours in all three nights.

range of timescales of the SF, we use the least squares method³ and fit Equation (2) to the observed SF after excluding the uncertain part beyond τ_{\max} .

The left panel of Figure 4 illustrates the best-fit functions (three thick curves) for the three observed *i*-band SFs while the corresponding best-fit parameters (i.e., σ_n , β , τ_d , and SF_∞) for all bands are tabulated in Table 1. The best-fit σ_n and β are relatively reliable with small differences among three nights (cf. Columns (6) and (7) in Table 1). Instead, both τ_d and SF_∞ , even with quite small best-fit errors, are actually very uncertain owing to both the limited baseline and the randomness nature of AGN variability, also indicated by the large dispersion of the best-fit values among three nights (cf. Columns (8) and (9) in Table 1).

Comparing the reported photometric uncertainties to our best-fit σ_n (the left panel of Figure 4 and Table 1), we find that McHardy et al. (2023) may slightly overestimate the photometric uncertainties, while Montano et al. (2022) may somewhat underestimate them. There-

fore, we decide to use the best-fit σ_n in each band to determine τ_{\min} for the corresponding band. Practically, we select τ_{\min} such that $SF_{\text{obs}}(\tau_{\min}) = 2 \times \sqrt{2}\sigma_n$. Note that selecting $SF_{\text{obs}}(\tau_{\min}) = \sqrt{x} \times \sqrt{2}\sigma_n$, the noise contribution to the true SF at τ_{\min} reaches a fraction of $\sqrt{x/(x-1)} - 1$, i.e., $\simeq 41\%$, $\simeq 10\%$, $\simeq 6\%$ for $x = 2, 6, 9$, respectively.

Although we deem that at timescales between τ_{\min} and τ_{\max} the SF should have been measured fairly accurately, a timescale range narrower than $[\tau_{\min}, \tau_{\max}]$ suggested here is required by a more conservative consideration because (1) the SF with a smaller τ_{\max} would be less affected by the limited baseline and (2) the SF with a larger τ_{\min} would further decrease the noise contribution at τ_{\min} , which is still as high as $\simeq 15\%$ ($= SF_{\text{obs}}/SF_{\text{true}} - 1$) given our selection of $SF_{\text{obs}}(\tau_{\min}) = 2 \times \sqrt{2}\sigma_n$.

In the right panel of Figure 4, we show the so-called true SFs (symbols) and the corresponding best-fit ones (curves) after subtracting the best-fit noise term, σ_n , from the observed SFs and the corresponding best-fit ones, respectively. A few unfit data points at $\tau > \tau_{\max}$ that are subject to the limited baseline are excluded.

³ LsqFit.jl: <https://github.com/JuliaNLSolvers/LsqFit.jl>

Comparing to the DRW prediction with $\beta = 1$, the true SFs in all three nights (and in all four bands; Table 1) have similar short-term slopes, $\beta \simeq 1.8$, demonstrating prominent departures from the DRW process at timescales shorter than \sim hours. Note that the residual noise at $\tau \lesssim 200$ s still induces large fluctuations in the true SF and even a systematical offset from the best-fit one. Hereafter, the true SF always indicates the observed one subtracted the best-fit noise term.

2.3. Color Variations

The SF provides the timescale-dependent variation property in a single band, while the CV highlights more subtle timescale-dependent variation property between two bands. In terms of a so-called quantity θ , defined in Sun et al. (2014), the timescale-dependent CV was originally presented in the magnitude space by Sun et al. (2014, see also Zhu et al. 2016) and also in the flux space by Cai et al. (2016). Later on, simplifying the analysis of the CV was upgraded by Zhu et al. (2018) and Cai et al. (2019) in the flux space and the magnitude space for local Seyfert galaxies and quasars, respectively.

It is worth noting that analyzing the CV in the magnitude space is highly immune to the intrinsic host extinction but can be subject to the contamination of the host emission and thus is more applicable to quasars whose host emission is negligible. However, for Seyfert galaxies and low-luminosity AGNs, such as NGC 4395, with significant host contribution, analyzing the CV in the flux space can naturally remove the host component, though the resulting color can be somewhat (timescale-independent) offset by the extinction difference between two given bands.

Here, we briefly outline the basic procedure for the CV in both the flux and magnitude spaces ($C_{f/m}$). Figure 5 exemplifies the CV using the i - and z -band FNT-1 light curves because (1) these two bands suffer less from the contamination of broad emission lines (Figure 1) and (2) the resultant CV is the most significant (Section 3.2).

Given two arbitrary light curves with superscripts “ r ” and “ b ” representing the redder and bluer bands, respectively,

(i) re-bin the two light curves such that they have photometric measurements (f_i or m_i) and associated uncertainties (σ_i) at the same instants (t_i), as we discussed in Section 2.1;

(ii) calculate the flux (magnitude) differences between the same two instants of two bands, e.g., $\Delta f^r(\tau) = f_i^r - f_j^r$ and $\Delta f^b(\tau) = f_i^b - f_j^b$ for the same $\tau = |t_i - t_j|$, forming C_n^2 data pairs, $\{\dots, [\Delta f^b(\tau), \Delta f^r(\tau)], \dots\}$;

(iii) perform a so-called 3σ -cut to exclude data pairs with statistically insignificant variations, i.e., requiring

$\sqrt{(\Delta f^b)^2 + (\Delta f^r)^2} > 3 \times \sqrt{\Sigma_i^2 + \Sigma_j^2}$ where a global photometric uncertainty at the i/j instant, being composed of the photometric uncertainties in the two bands, is given by $\Sigma_{i/j} = \sigma_{i/j}^b \sigma_{i/j}^r / \sqrt{(\sigma_{i/j}^b \sin \phi)^2 + (\sigma_{i/j}^r \cos \phi)^2}$ with $\tan \phi \equiv \Delta f^r / \Delta f^b$ (cf. Sun et al. 2014 and their Figure 1 for details). Note that applying the 3σ -cut primarily decreases the number of data pairs at shorter timescales (i.e., from the black dashed histogram to the blue dotted histogram in the panel (b) of Figure 5);

(iv) assess the CV according to, in the flux space,

$$C_f(\tau) = \frac{\Delta f^r(\tau)}{\Delta f^b(\tau)} = \frac{f_i^r - f_j^r}{f_i^b - f_j^b}, \quad (4)$$

where f_i is in units of erg/s/cm²/Å, or in the magnitude space,

$$C_m(\tau) = \frac{\Delta m^r(\tau)}{\Delta m^b(\tau)} = \frac{m_i^r - m_j^r}{m_i^b - m_j^b}, \quad (5)$$

shown in the panels (c) and (d) of Figure 5, respectively;

(v) take the median value of a set of $C_{f/m}$ within a certain range of timescales after excluding negative or unphysical $C_{f/m}$, that is, requiring that AGNs behave brighter or fainter simultaneously in both bands and avoiding bias by the extreme $C_{f/m}$. Note that requiring $C_{f/m} > 0$ only removes a few data pairs, again mostly at shorter timescales (i.e., from the blue dotted histogram to the magenta solid histogram in the panel (b) of Figure 5);

and (vi) utilize the random subset selection method following Zhu et al. (2018) to estimate the uncertainty for the median CV derived in the step (v), that is, generating 10^3 realizations of mock light curves (with replacement), repeating steps (i) to (v), and taking the standard deviation of the bootstrapped median CV as the desired 1σ uncertainty.

The final data pairs satisfying both the 3σ -cut and $C_{f/m} > 0$ are used to calculate the CV as a function of timescales in the flux and magnitude space, shown as the open/filled circles in the panels (c) and (d) of Figure 5, respectively. Since the CV can be approximated by the ratio of two SFs and so fluctuates more strongly than the SF, a larger bin size of 0.2 dex is adopted to average $C_{f/m}$. In panels (c) and (d) of Figure 5, there are two horizontal dashed lines, beneath and beyond which the CV behaves BWB and redder-when-bright (RWB), respectively. In the magnitude space, $C_m = 1$ is always the separation between BWB and RWB. Instead, in the flux space, the same separation depends on the relative contribution between two given bands and can be roughly estimated as $C_f \simeq (\bar{f}^r / \bar{f}^b) C_m = \bar{f}^r / \bar{f}^b$ where \bar{f}^r and \bar{f}^b are the mean flux densities in the redder and bluer bands (see Equation (4) of Sun et al. 2014).

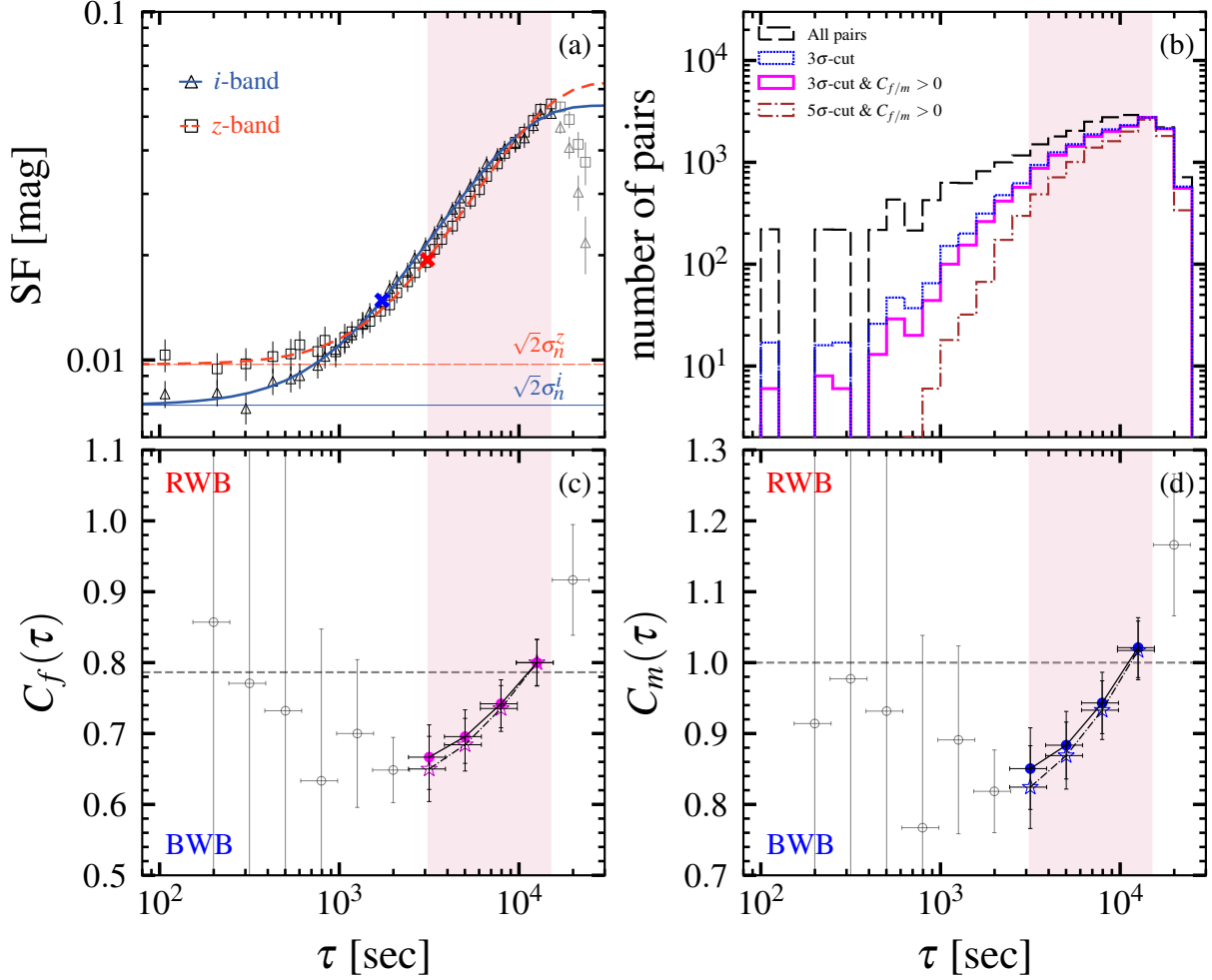


Figure 5. Using the *i*- and *z*-band FNT-1 light curves of NGC 4395, illustrated are the corresponding observed SFs (panel (a); Section 2.2), distributions of data pairs (panel (b); Section 2.3), and CVs in the flux/magnitude space (panel (c/d); Section 2.3). Similar to Figure 4, the panel (a) displays both the observed *i*- and *z*-band SFs (open symbols), the noise levels in terms of the best-fit $\sqrt{2}\sigma_n$ (two horizontal lines), the minimal timescales where $SF_{\text{obs}} = 2 \times \sqrt{2}\sigma_n$ adopted for each band (cross symbols), and a shaded region for the proper range of timescales, deemed to be little affected by both the photometric uncertainties and the limited baseline (Section 2.3.1). The panel (b) shows distributions of data pairs: all pairs (dashed histogram), pairs after 3 σ -cut (dotted histogram), pairs satisfying both 3 σ -cut and $C_{f/m} > 0$ (solid histogram), and pairs satisfying both 5 σ -cut and $C_{f/m} > 0$ (dot-dashed histogram). The panel (c/d) presents, using pairs satisfying both 3 σ -cut and $C_{f/m} > 0$, the CVs in the flux/magnitude space (circles), while highlighted are a subset possessing a definite timescale-dependent within the shaded region (blue filled circles). For comparison, shown are the CVs (open asterisks) implied by pairs satisfying both 5 σ -cut and $C_{f/m} > 0$. Besides, two horizontal dashed lines in the two bottom panels separate the CVs into the BWB and RWB regions.

For $3 \times 10^3 \text{ s} \lesssim \tau \lesssim 10^4 \text{ s}$, the *i* versus *z* CVs of NGC 4395 in both the flux and magnitude spaces all behave BWB and are clearly timescale-dependent, that is, the BWB trend is more prominent at shorter timescales. Instead, once $\tau \lesssim 3 \times 10^3 \text{ s}$, the BWB trend gradually disappears with decreasing timescales. This is mainly attributed to the increasing dominance of the photometric uncertainty with decreasing timescales as simulated by Zhu et al. (2018, cf. their Figure 5). On the other aspect of $\tau \gtrsim 10^4 \text{ s}$, the CV seemingly behaves RWB and becomes more redder at longer timescales. Although some

mechanisms, such as the inward propagation of the perturbation over the accretion disk, could result in a RWB trend at longer timescales, this RWB trend at $\tau \gtrsim 10^4 \text{ s}$ is not conclusive because it could be heavily subject to the limited baseline as indicated by the rapid drops of both the SF and the number of data pairs, shown in the panel (a) and (b) of Figure 5, respectively.

2.3.1. A Proper Range of Timescales for the CV

As introduced above, the CVs over all available timescales are globally complicated and definitely af-

ected by the photometric uncertainty and the limited baseline at shorter and longer timescales, respectively. We therefore seek a unique way to select a proper range of timescales in which the derived CVs are less affected by both the photometric uncertainty and the limited baseline.

We rely on the observed SF for which we have determined a proper range of timescales in a single band (Section 2.2). For instance, assuming $[\tau_{\min}^i, \tau_{\max}^i]$ and $[\tau_{\min}^z, \tau_{\max}^z]$ are the proper ranges of timescales for the observed i - and z -band SFs, respectively, we thus treat $[\max\{\tau_{\min}^i, \tau_{\min}^z\}, \min\{\tau_{\max}^i, \tau_{\max}^z\}]$ as the proper range of timescales (cf. the shaded regions in Figure 5) for the i versus z CV.

By increasing the 3σ -cut to a stricter 5σ -cut, we confirm that the resultant CVs within the proper range of timescales are also consistent (Figure 5), and thus we adopt the 3σ -cut in the following discussions.

3. DISCUSSIONS

3.1. Structure Function (SF)

3.1.1. Prominent departures from the DRW process at the intermediate-mass scale

Although departures from the DRW process have been reported in AGNs at the supermassive scale (e.g., Mushotzky et al. 2011; Kelly et al. 2014; Kasliwal et al. 2015; Simm et al. 2016; Zhu et al. 2016; Guo et al. 2017; Stone et al. 2023), a departure alike has never been reported in any AGN at the intermediate-mass scale. Thanks to the high-quality (i.e., high cadence, long baseline, small photometric uncertainties) light curves provided by current surveys, we now have the chance to study the variability properties of an IMBH, NGC 4395, at timescales of minutes to hours (Burke et al. 2020; McHardy et al. 2023; Montano et al. 2022).

As tabulated in Table 1 for all bands and nights, all values of the best-fit β for NGC 4395 indicate significant departures from the DRW process at the intermediate-mass scale for the first time. For the g , r , i , and z bands, the mean β over three nights are $\simeq 1.80 \pm 0.05$, $\simeq 1.80 \pm 0.07$, $\simeq 1.77 \pm 0.09$, and $\simeq 1.82 \pm 0.16$, respectively, which are all inconsistent with $\beta \equiv 1$ implied by the DRW process. After subtracting the best-fit σ_n and excluding unfit data points, the right panel of Figure 4 illustrates the i -band true SFs of NGC 4395 observed in three nights. Regardless of the large differences in both τ_d and SF_∞ between the three nights of observation, owing to both the limited baseline and the randomness nature of AGN variability, almost the same short-term slopes at timescales shorter than \sim hours are found in those SFs of NGC 4395 and are all steeper than implied by the DRW process.

Previously, Burke et al. (2020) analyzed the I_C -band⁴ TESS light curve (\sim month-long and 30-minute-cadence) of NGC 4395 and found $\beta \simeq 0.94 \pm 0.08$, which is consistent with the DRW process. Using their light curve, the top panel of Figure 6 shows the observed TESS SF (squares) which can be fitted by Equation (2) with $\beta \simeq 0.96 \pm 0.05$. Since the TESS SF is limited to timescales $\gtrsim 2 \times 10^3$ s and strongly affected by photometric uncertainties at timescales $\lesssim 10^4$ s, the β derived from the TESS SF should have only characterized the slope of SF around $\sim 10^4$ s and can not represent the true β at $\lesssim 10^4$ s, while we can use the much higher cadence and more accurate light curves from Montano et al. (2022) and McHardy et al. (2023).

In the top panel of Figure 6, the observed TESS SF (squares) is significantly lower than the FNT-1 SF (circles), probably owing to the large TESS pixels (21 arcsec), which results in huge galaxy contamination. Here, after subtracting the best-fit σ_n , scaling the “true” TESS SF horizontally to the same level as the FNT-1 SF at $\sim 10^4$ s (diamonds) forms a stitched global SF spanning \sim minute to \sim month for NGC 4395. This stitched SF suggests that its slope may change from $\beta \simeq 1.8$ below $\sim 10^4$ s, through $\beta \simeq 1.0$ around, and to $\beta \simeq 0.7$ beyond, to be justified by future homogeneous observations on NGC 4395. Even quite uncertain, this comparison between the TESS and FNT-1 SFs of NGC 4395 is suggestive and could stimulate more future observations on it spanning timescales over \sim minute to \sim month, and even \sim year.

To obtain a true global SF for NGC 4395, longer (as long as several months) and denser (as short as ~ 100 s) monitoring should be conducted repeatedly. Using \sim month long light curve of NGC 4395, Burke et al. (2020) find a damping timescale of $1.4_{-0.5}^{+1.9}$ days. The 1σ upper limit for the damping timescale is already 3.3 days, suggesting that a single one-month-long light curve is far from any firm conclusion on the true intrinsic damping timescale for NGC 4395 (e.g., Hu et al. 2023; Zhou et al. 2024). According to Hu et al. (2023, cf. their Figure 8), if the true damping timescale is 1.4 days for NGC 4395, the retrieved damping timescale has $\sim 40\%$ (1σ confidence level) dispersion given a single light curve with a one-month-long baseline. For NGC 4395, the dispersion can be reduced to $\sim 10\%$ (1σ confidence level) only if the baseline of a continuing monitoring has been

⁴ The TESS bandpass, i.e., 6000 Å to 1 μ m (Ricker et al. 2015), is much wider than but is centered on the Johnson-Cousins I_C band, whose effective wavelength is 7980 Å (Bessell 2005). Therefore, we compare the i - and I_C -band SFs.

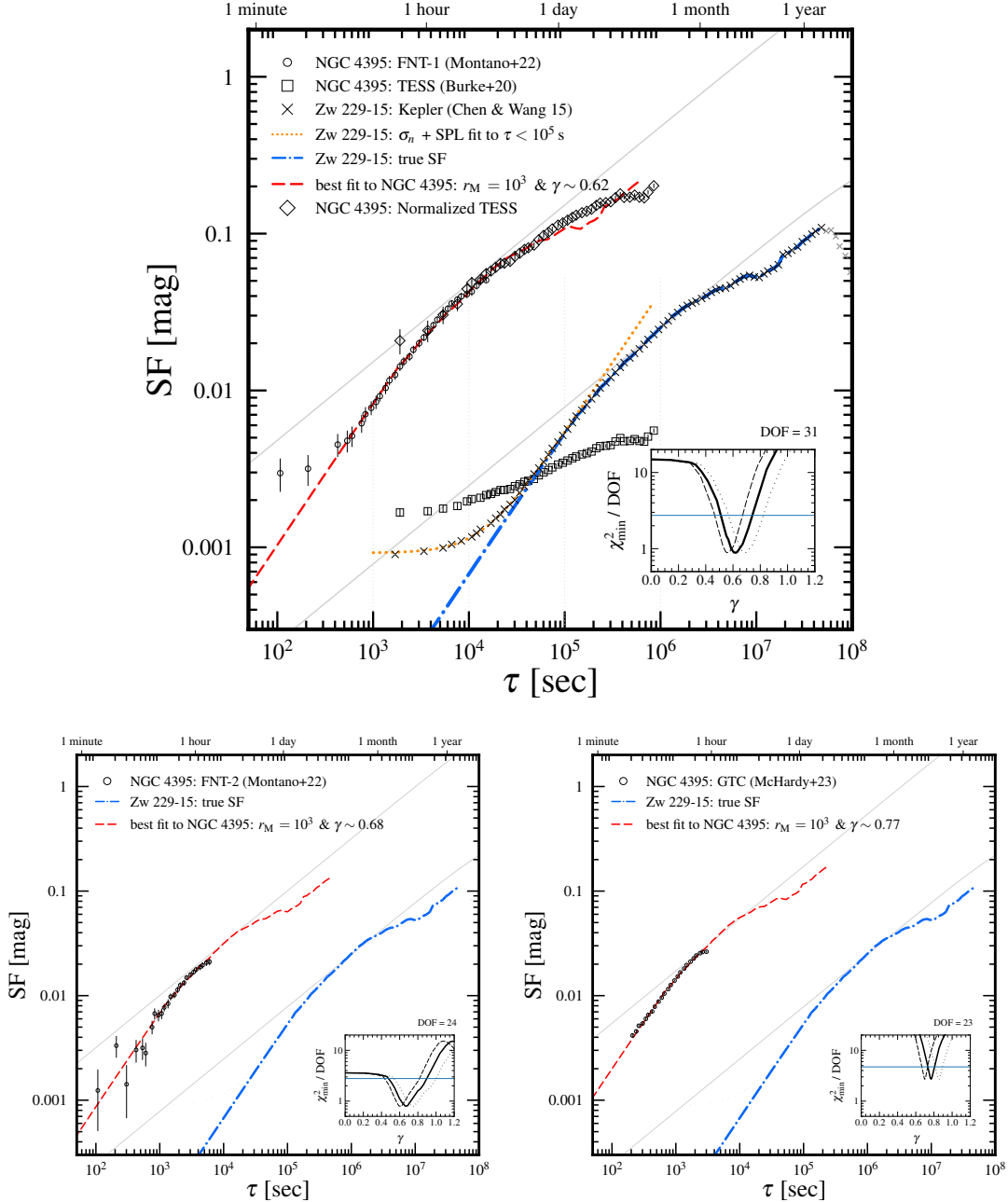


Figure 6. Top panel: SFs of NGC 4395 ($M_{\text{BH}} \simeq 10^4 M_{\odot}$) at the intermediate-mass scale are compared to that of Zw 229-15 ($M_{\text{BH}} \simeq 10^7 M_{\odot}$) at the supermassive scale. For NGC 4395, the true i -band FNT-1 SF (Montano et al. 2022, circles) is shown with the observed I_C -band TESS SF (Burke et al. 2020, squares) as well as the corresponding normalized “true” TESS SF (diamonds). For Zw 229-15, its *Kepler* light curve stitched by Chen & Wang (2015) is used to derive the observed SF (crosses), a short-term portion (i.e., $\tau < 10^5$ s) of which is fitted with a noise term (σ_n) plus a single power-law (SPL) function (i.e., the dotted curve for the best σ_n + SPL fit with $\beta \simeq 1.82 \pm 0.01$, that has been extended beyond $\tau \sim 10^5$ s to highlight the complexity of the true SF more than a single SPL). After removing the noise contribution, the true SF of Zw 229-15 (the dot-dashed curve) is scaled horizontally by a factor of r_M^{γ} before fitted vertically to the true FNT-1 SF of NGC 4395, where r_M is the mass ratio of Zw 229-15 to NGC 4395 and γ is the mass index. The inset shows the minimal chi-square, χ^2_{\min} , divided by the degree of freedom (DOF), as a function of γ for $r_M = 10^3$ (solid curve), $r_M/2$ (dotted curve), and $2r_M$ (dashed curve). A blue horizontal line in the inset represents the 3σ confidence level given the DOF. The best-fit SF to NGC 4395 (the dashed curve) is presented for $r_M = 10^3$ and the optimized $\gamma \sim 0.62$. Interestingly, the true FNT-1 and “true” TESS SFs of NGC 4395 across $\sim 10^3$ s to $\sim 10^6$ s is found to be in nice agreement with the scaled SF of Zw 229-15, suggesting a similar accretion physics in AGNs across different mass scales. For comparison, two light-gray thin lines tilted for $\beta = 1$ highlight prominent departures from the DRW process at short timescales. Bottom panels: same as the top panel but for fitting the true SF of Zw 229-15 to the FNT-2 (bottom-left panel) and GTC (bottom-right panel) SFs of NGC 4395. The fact that somewhat larger γ is preferred by a shorter baseline indicates a potential bias on γ induced by the shorter baseline.

increased to \sim year or a one-month-long monitoring has been repeated at least 10 times.

3.1.2. SFs of AGNs at the supermassive scale

The optical variability properties of individual AGNs (e.g., Mushotzky et al. 2011; Kasliwal et al. 2015; Simm et al. 2016; Zhu et al. 2018) and AGN samples (e.g., Arévalo et al. 2023a,b; Stone et al. 2023) at the supermassive scale have been extensively investigated in recent years. However, there are only a few AGNs possessing both sufficiently long (as long as several years) and high cadence (as short as \sim hour) monitoring such that the global variation properties across several orders of timescales can be unveiled, rather than a single typical damping timescale (τ_d), which is also uncertain owing to the limited baseline and cadence. Instead, we would directly compare the global SFs of several AGNs, mainly from the *Kepler* monitoring, at the supermassive scale to that of NGC 4395 at the intermediate-mass scale in order to investigate the accretion physics across different mass scales.

Benefiting from the sufficiently long (\sim years) and high cadence (\sim 30 minutes) *Kepler* monitoring in a broad bandpass from 4230 Å to 8970 Å (Koch et al. 2010), Mushotzky et al. (2011) first reported departures from the DRW process at timescales of $\sim 2 \times 10^4$ s (or ~ 6 hr) to $\sim 2 \times 10^6$ s (or ~ 1 month) in four AGNs at the supermassive scale. Among them, the Seyfert galaxy Zw 229-15 (at $z = 0.0275$ and with $M_{\text{BH}} \simeq 10^7 M_{\odot}$; Barth et al. 2011) has been observed in four quarters, within which β changes from $\simeq 1.48$ to $\simeq 1.65$; the Seyfert galaxy W2R 1904+37 (at $z = 0.089$ with $M_{\text{BH}} \simeq 10^{7.66} M_{\odot}$; Smith et al. 2018) has been observed in three quarters, within which changes from $\beta \simeq 1.30$ to $\simeq 1.38$; the Seyfert galaxy W2 1925+50 (at $z = 0.067$ with $M_{\text{BH}} \simeq 10^{8.04} M_{\odot}$; Smith et al. 2018) has been observed in three quarters, within which β changes from $\simeq 1.37$ to $\simeq 1.48$; and the Seyfert galaxy W2R 1858+48 has been observed in two quarters, within which β transitioned from $\simeq 1.44$ to $\simeq 1.49$. Except the last one, the other three AGNs, i.e., Zw 229-15, W2R 1904+37, and W2 1925+50, have years-long light curves stitched by Chen & Wang (2015)⁵ such that their global SFs are

achievable. Therefore, we mainly consider these three AGNs at the supermassive scale. One more AGN at the supermassive scale we consider even without sufficiently long and high cadence monitoring (with ~ 200 days-long and ~ 1 day-cadence according to Fausnaugh et al. 2016) is the famous Seyfert galaxy NGC 5548 (at $z = 0.017175$ with $M_{\text{BH}} \simeq 10^{7.59} M_{\odot}$; Pancoast et al. 2014) since it is the first individual AGN whose CVs between UV/optical are found to be timescale-dependent by Zhu et al. (2018) and are to be compared with that of NGC 4395 in Section 3.2. To compare with the *i*-band SFs of NGC 4395, we also use the *i*-band light curve for NGC 5548 from Fausnaugh et al. (2016).

Basic physical and observational properties are tabulated in Table 2 for the four AGNs at the supermassive scale. In the top panels of Figures 6 to 9, we show the observed SFs (crosses) for Zw 229-15, W2 1925+50, W2R 1904+37, and NGC 5548, respectively. For the two AGNs with the longest baselines, i.e., Zw 229-15 over $\simeq 3.3$ yrs and W2 1925+50 over $\simeq 2.8$ yrs, their SFs intuitively have at least two breaks near $\sim 10^{5-6}$ s and $\sim 10^{6-7}$ s, indicating that a single β could be not enough for describing their global SFs. Using a single power-law (SPL) function fitting to the SF in three distinct timescale ranges, we find that with increasing timescales β changes from $\simeq 1.8$, through $\simeq 1.3$, to $\simeq 0.7$ for both Zw 229-15 and W2 1925+50 (see Table 2 for the selected timescale ranges and the corresponding best-fit β). Note that owing to the significance of the noise contribution within the smallest timescale range, a noise term has been included in the fit, that is, the nominated $\sigma_n + \text{SPL}$ fit (cf. the dotted curves in Figures 6 and 7 for Zw 229-15 and W2 1925+50, respectively).

Similarly, we have performed the $\sigma_n + \text{SPL}$ fit to the observed SFs of the other two AGNs at the supermassive scale, i.e., W2R 1904+37 (Figure 8) and NGC 5548 (Figure 9). However, likely owing to their relatively short baselines, only a single short-term slope for each of them can be determined.

Interestingly, at timescales shorter than $\sim 10^{5-6}$ s, the short-term slopes of SFs of the four AGNs at the supermassive scale are all around $\beta \simeq 1.8$ (Table 2), which is also nicely consistent with that of NGC 4395 at $\tau \lesssim 10^4$ s (Section 3.1.1 and the right panel of Figure 4). The consistency of the short-term slopes of the SFs among AGNs across a broad mass scale suggests a similar accretion physics at work.

The five AGNs we consider here show almost the same departures from the DRW process. Mushotzky et al. (2011) suggest the departure from the DRW process may be related to the magneto-rotational instability in terms of a similar high-frequency slope of PSDs of the mass

⁵ The light curves of W2R 1858+48 can not be stitched according to Chen & Wang (2015). Instead, they stitched the light curves of CGRaBS J1918+4937. However, we do not consider CGRaBS J1918+4937 since it is likely a BL Lac object without a reliable BH mass (Smith et al. 2018).

Table 2. Basic physical and observational properties of four AGNs at the supermassive scale.

AGN Name	M_{BH} ($10^7 M_{\odot}$)	λ_{Edd}	Δt_{min}	Δt_{max} (yr)	σ_n (10^{-2} mag)	β		
						$[\tau_1, \tau_2]/(\text{s})$	$[\tau_2, \tau_3]/(\text{s})$	$[\tau_3, \tau_4]/(\text{s})$
(1)	(2)	(3)	(4)	(5)	(6)	(7)	(8)	(9)
Zw 229-15	$\simeq 1$	0.050	30 min	$\simeq 3.30$	0.07 ± 0.01	$\simeq 1.82 \pm 0.01$ [$10^3, 10^5$]	$\simeq 1.27 \pm 0.01$ [$10^5, 10^6$]	$\simeq 0.73 \pm 0.01$ [$10^6, 5 \times 10^7$]
W2 1925+50	$\simeq 10$	0.013	30 min	$\simeq 2.79$	0.11 ± 0.01	$\simeq 1.83 \pm 0.01$ [$10^3, 5 \times 10^5$]	$\simeq 1.30 \pm 0.01$ [$5 \times 10^5, 10^7$]	$\simeq 0.70 \pm 0.01$ [$10^7, 5 \times 10^7$]
W2R 1904+37	$\simeq 5$	0.089	30 min	$\simeq 2.54$	0.10 ± 0.01	$\simeq 1.83 \pm 0.01$ [$10^3, 10^6$]	-	-
NGC 5548	$\simeq 5$	0.050	$\simeq 1$ day	$\simeq 0.58$	0.36 ± 0.10	$\simeq 1.72 \pm 0.16$ [$10^4, 5 \times 10^5$]	-	-

NOTE— Column (1): the names of AGNs at the supermassive scale. Column (2): the BH mass in units of $10^7 M_{\odot}$, taken from Barth et al. (2011) for Zw 229-15, from Smith et al. (2018) for W2 1925+50 and W2R 1904+37, and from Fausnaugh et al. (2016) for NGC 5548. Column (3): the Eddington ratio taken from the same references as the BH mass. Column (4): the minimal cadence given by the *Kepler* mission for the first three AGNs, while the median one for NGC 5548 taken from Fausnaugh et al. (2016). Column (5): the maximal available baseline in units of year, estimated using the stitched *Kepler* light curves from Chen & Wang (2015) and the *i*-band one from Fausnaugh et al. (2016) for NGC 5548. Column (6): the best-fit noise level. Columns (7) to (9): the best-fit SPL slopes as well as the corresponding 1σ uncertainties within three timescale ranges given by $[\tau_i, \tau_{i+1}]$ in units of second. For the smallest timescale range, $[\tau_1, \tau_2]$, a noise level presented in Column (6) has been included in the fit, while a single SPL function is used for the other two timescale ranges.

accretion rate simulated by Reynolds & Miller (2009). Regardless of the fundamental problem suffered by simulations to convert the disk turbulence into radiation, we unveil more complicated structures in the global SFs of Zw 229-15 and W2 1925+50, suggesting that a global comparison between simulations and the data is necessary and essential.

3.1.3. Comparing SFs of AGNs across the intermediate-mass to supermassive scales

Rather than considering a single typical damping timescale of the SF, directly comparing the global SFs of two AGNs to establish the dependence of timescales on BH mass are very informative, even with two AGNs only at a time. To do so, we should use their true SFs derived after having subtracted the noise contribution around the shortest timescales from the observed ones. For NGC 4395, its true SFs in three nights have been introduced in Section 2.2.1 and illustrated in the right panel of Figure 4 (see also circles in Figures 6 to 9). For the four supermassive AGNs, especially Zw 229-15 and W2 1925+50 whose global SFs break at more than a damping timescale (Section 3.1.2), we use a $\sigma_n + \text{SPL}$ function to fit their observed SFs at timescales smaller than τ_2 , which broadly indicates the shortest breaking timescale of the SF (Table 2). Then, the corresponding

true SFs are obtained after subtracting the best-fit σ_n from the observed ones and are illustrated as the dot-dashed lines in Figures 6 to 9.

To determine the timescale-mass scaling, $\tau \propto r_{\text{M}}^{\gamma}$, where r_{M} is the mass ratio of an AGN at the supermassive scale to NGC 4395 (cf. Tables 2 and 3) and γ is the mass index, we fit the true SF of an AGN at the supermassive scale to that of NGC 4395 at the intermediate scale. For a given r_{M} , the true SF of an AGN at the supermassive scale is then scaled horizontally by a factor of r_{M}^{γ} for a series of γ between 0 and 1.2, before fitting vertically to the true SF of NGC 4395. Note that for the GTC monitoring on NGC 4395, only data points at $\tau \gtrsim 200$ s are used in the fit to avoid the clear residual noise (see the right panel of Figure 4).

For each r_{M} and γ , the fit results in a minimal reduced chi-square, $\chi_{\text{min}}^2/\text{DOF}$, where χ_{min}^2 is the minimal chi-square and DOF is the degree of freedom. The insets of Figures 6 to 9 illustrate $\chi_{\text{min}}^2/\text{DOF}$ as a function of γ for our fiducial r_{M} and two more mass ratios, i.e., $r_{\text{M}}/2$ and $2r_{\text{M}}$. The fiducial r_{M} corresponds to the ratio of the measured BH masses (Table 2), while the other two mass ratios are considered for illustrating the effect induced by the measured uncertainty of the BH mass. For each r_{M} , we determine a best γ corresponding to the minimum of $\chi_{\text{min}}^2(\gamma)/\text{DOF}$, i.e., $\text{Min}[\chi_{\text{min}}^2/\text{DOF}]$, and

Table 3. Comparing the true SFs of four AGNs at the supermassive scale to the true SF of NGC 4395 observed in three nights at the intermediate-mass scale to determine the best γ for $\tau \propto M^\gamma$.

AGN Name	r_M	NGC 4395	DOF	$\Delta\chi^2(\text{DOF})$	$\text{Min}[\chi_{\text{min}}^2/\text{DOF}]$	best γ		
						$r_M/2$	r_M	$2r_M$
(1)	(2)	(3)	(4)	(5)	(6)	(7)	(8)	(9)
Zw 229-15 (Figure 6)	10^3	FNT-1	31	57.40	0.88	$\sim 0.69^{+0.13}_{-0.12}$	$\sim 0.62^{+0.11}_{-0.10}$	$\sim 0.56^{+0.11}_{-0.10}$
		FNT-2	24	47.76	0.79	$\sim 0.76^{+0.22}_{-0.20}$	$\sim 0.68^{+0.22}_{-0.20}$	$\sim 0.62^{+0.20}_{-0.18}$
		GTC	23	46.36	2.70	$\sim 0.86^{+0.04}_{-0.03}$	$\sim 0.77^{+0.03}_{-0.03}$	$\sim 0.70^{+0.03}_{-0.03}$
W2 1925+50 (Figure 7)	10^4	FNT-1	31	57.40	0.54	$\sim 0.78^{+0.05}_{-0.07}$	$\sim 0.72^{+0.11}_{-0.06}$	$\sim 0.67^{+0.05}_{-0.06}$
		FNT-2	24	47.76	0.87	$\sim 0.86^{+0.09}_{-0.30}$	$\sim 0.80^{+0.08}_{-0.28}$	$\sim 0.74^{+0.08}_{-0.26}$
		GTC	23	46.36	2.84	$\sim 0.93^{+0.02}_{-0.05}$	$\sim 0.86^{+0.02}_{-0.05}$	$\sim 0.80^{+0.02}_{-0.04}$
W2R 1904+37 (Figure 8)	5×10^3	FNT-1	31	57.40	1.10	$\sim 0.92^{+0.03}_{-0.03}$	$\sim 0.85^{+0.01}_{-0.03}$	$\sim 0.78^{+0.02}_{-0.02}$
		FNT-2	24	47.76	0.58	$\sim 1.03^{+0.04}_{-0.37}$	$\sim 0.95^{+0.03}_{-0.33}$	$\sim 0.87^{+0.04}_{-0.03}$
		GTC	23	46.36	1.70	$\sim 1.12^{+0.01}_{-0.02}$	$\sim 1.03^{+0.01}_{-0.02}$	$\sim 0.95^{+0.01}_{-0.01}$
NGC 5548 (Figure 9)	5×10^3	FNT-1	31	57.40	0.43	$\sim 0.65^{+0.04}_{-0.05}$	$\sim 0.59^{+0.04}_{-0.04}$	$\sim 0.55^{+0.03}_{-0.04}$
		FNT-2	24	47.76	0.67	$\sim 0.75^{+0.07}_{-0.75}$	$\sim 0.68^{+0.07}_{-0.68}$	$\sim 0.63^{+0.06}_{-0.63}$
		GTC	23	46.36	0.92	$\sim 0.83^{+0.02}_{-0.03}$	$\sim 0.76^{+0.02}_{-0.02}$	$\sim 0.70^{+0.02}_{-0.02}$

NOTE— Column (1): the names of AGNs at the supermassive scale. Column (2): the fiducial mass ratios of AGNs at the supermassive scale to that of NGC 4395 ($M_{\text{BH}} \simeq 10^4 M_\odot$). Column (3): the abbreviations indicate observations on NGC 4395 in three nights. Column (4): the degree of freedom (DOF) in each fit. Column (5): the expected change in χ^2 given a 3σ confidence level, estimated following Wall & Jenkins (2012, cf. their Section 5.3.1). Column (6): the minimum of $\chi_{\text{min}}^2(\gamma)/\text{DOF}$, where a minimal χ_{min}^2 is determined for each given r_M and γ . Changing r_M results in distinct best γ , but the corresponding value of $\text{Min}[\chi_{\text{min}}^2(\gamma)/\text{DOF}]$ is the same. Columns (7) to (9): the best values for γ corresponding to the $\text{Min}[\chi_{\text{min}}^2(\gamma)/\text{DOF}]$, as well as the associated 3σ uncertainties, given three fixed values for the mass ratio, i.e., r_M , $r_M/2$, and $2r_M$. Highlighted in boldface are the most plausible values for γ we suggest according to the available data: both the *Kepler* light curves for Zw 229-15 and W2 1925+50 as well as the FNT-1/2 light curve for NGC 4395 are all or nearly the longest.

assess the associated 3σ confidence level corresponding to $\text{Min}[(\chi_{\text{min}}^2 + \Delta\chi^2)/\text{DOF}]$, where $\Delta\chi^2$ is related to the DOF (Wall & Jenkins 2012, cf. their Section 5.3.1). All fitting results are tabulated in Table 3.

From Figures 6 to 9, we compare the SFs of four AGNs at the supermassive scale to the three-night SFs of NGC 4395 at the intermediate-mass scale. Overall, the best γ are all larger than 0.5 and up to ~ 1.1 . On one hand, there is a degeneracy between r_M and γ , that is, the larger r_M the smaller γ . If the mass ratio increases by a factor of four, i.e., from $r_M/2$ to $2r_M$, the resultant γ decreases by ~ 0.13 . On the other hand, the best γ surprisingly depends on the baseline of the light curve.

For all four AGNs at the supermassive scale, the resultant γ is larger by ~ 0.16 when the baseline of NGC 4395 decreases from 6.7 hr of FNT-1 to 2.2 hr of GTC. This strongly suggests that the larger γ inferred from the comparison to a shorter baseline of NGC 4395 is likely a bias. A shorter baseline results in a smaller but unreal break timescale on the SF (cf. the *i*-band SFs of

NGC 4395 in the right panel of Figure 4 and the corresponding best-fit τ_d in Table 1).

Similarly, when comparing the SFs of AGNs at the supermassive scale to the FNT-1 SF of NGC 4395, a shorter baseline broadly gives rise to larger γ (Table 3). Figure 10 illustrates a direct comparison on the SFs of AGNs at the supermassive scale to highlight the effect of the limited baseline. For Zw 229-15 and W2 1925+50, their baselines are almost the longest and the resultant γ are comparable considering the fit uncertainties. Note that the reported BH mass of W2R 1904+37 is similar to that of NGC 5548 and smaller than that of W2 1925+50. However, the break timescale of the SF of W2R 1904+37 is clearly much larger than that of NGC 5548 and likely even larger than that of W2 1925+50. This suggests that the reported BH mass of W2R 1904+37 may have been underestimated. If the BH mass of W2 1925+50 were larger, the resultant γ would be smaller and so likely be consistent with those inferred by using the SFs of Zw 229-15 and W2 1925+50. Last for NGC 5548, its baseline is too short to reach any firm conclusion, even

the current fit gives a γ comparable to those inferred by using the SFs of Zw 229-15 and W2 1925+50.

Consequently, we suggest that the real γ could be around $\sim 0.6 - 0.8$ according to the comparisons between the SFs of Zw 229-15 (and W2 1925+50) and the FNT-1/2 SF of NGC 4395.

Last but not least, we note that the observed TESS SF of NGC 4395 occupies a timescale range from $\sim 10^3$ s to $\sim 10^6$ s, even though its SF level is extremely lower than the FNT-1 SF (Figure 6). We make a tentative extension of the FNT-1 SF by extracting the “true” TESS SF and normalizing it to the true FNT-1 SF at $\sim 10^4$ s (open diamonds in Figure 6). Thus, the FNT-1 SF was extended to $\sim 10^6$ s. Astonishingly, we find a global consistency between the extended SF for NGC 4395 and the scaled SF for Zw 229-15 (with $\gamma \sim 0.62$). Note that the timescales at which the SF slope begins to depart from the DRW process, i.e., ~ 0.3 days for NGC 4395 and ~ 10 days for Zw 229-15, are consistent with that predicted by Sun et al. (2020a), again suggesting a similar accretion process and variability in AGNs across different mass scales. In the future, directly extending the FNT-like observations on NGC 4395 from 1-2 days to \sim month would be valuable in learning the accretion physics. Nevertheless, the SFs of AGNs at different mass scales could not be simply scalable, and any dependence or not of the slope on M_{BH} or other AGN parameters would be worthy of further investigation (Simm et al. 2016).

3.1.4. A new timescale-mass scaling

The timescale-mass scaling relation, $\tau \propto M^\gamma$, has been extensively studied over the past decade. However, the mass indexes, γ , have not been agreed upon, and change from $\gamma < 0.5$ for a weak dependence, e.g., $\tau_{\text{d}} \propto M_{\text{BH}}^{\sim 0}$ (Simm et al. 2016), $\tau_{\text{d}} \propto M_{\text{BH}}^{0.05 \pm 0.03} \lambda_{\text{Edd}}^{-0.09 \pm 0.02}$ (Suberlak et al. 2021), $\tau_{\text{d}} \propto M_{\text{BH}}^{0.14 \pm 0.12} \lambda_{\text{Edd}}^{-0.08 \pm 0.10}$ (MacLeod et al. 2010), $\tau_{\text{d}} \propto M_{\text{BH}}^{0.38 \pm 0.15}$ (Kozłowski 2016), and $\tau_{\text{d}} \propto M_{\text{BH}}^{0.38 \pm 0.05}$ (Burke et al. 2021), to $\gamma > 0.5$ for a strong dependence, e.g., $\tau_{\text{d}} \propto M_{\text{BH}}^{0.61 \pm 0.47} \lambda_{\text{Edd}}^{-0.42 \pm 0.28}$ (Kelly et al. 2009), $\tau_{\text{d}} \propto M_{\text{BH}}^{0.62} \lambda_{\text{Edd}}^{0.48}$ (Guo et al. 2017), and $\tau_{\text{d}} \propto M_{\text{BH}}^{0.55-0.65} \lambda_{\text{Edd}}^{0.35-0.3}$ (Arévalo et al. 2023a). Note all these works adopt the DRW damping timescale, τ_{d} .

Utilizing the *Zwicky Transient Facility* (ZTF) g -band light curves of 4770 quasars, Arévalo et al. (2023a) grouped these light curves into 26 independent bins of M_{BH} and λ_{Edd} , and calculated a low-resolution g -band power spectrum for each bin using Mexican hat filter (Arévalo et al. 2012). They approximated these power spectra by using a straightforward analytical model, i.e., a bending power-law model, which incor-

porates a break timescale, τ_{d} , and two slopes below and above τ_{d} , and favored a steep slope below τ_{d} , indicating a departure from the DRW process. Besides, with $\tau_{\text{d}} \propto M_{\text{BH}}^{0.55-0.65} \lambda_{\text{Edd}}^{0.35-0.3}$, Arévalo et al. (2023a) found that all power spectra can be simplified to a universal power spectrum. Their work depends on the assumed model with two slopes to account for the observed ZTF power spectra, which probe the variation at timescales of ~ 3 days to 300 days. However, according to what we have discussed in Section 3.1.2, the global SFs of AGNs may have two or more breaks, which are worthy of justification with the arrival new time-domain surveys.

Being different from all previous works, we do not use the single damping timescale (τ_{d}) but utilize the whole variation properties across nearly all available timescales. Interestingly, our mass index agrees well with that derived by Arévalo et al. (2023a) using a different method. Furthermore, our mass index is quite consistent with the prediction of the simple static standard thin disk, i.e., $\tau_{\text{d}} \propto M_{\text{BH}}^{0.5}$, assuming τ_{d} is related to the thermal timescale, and is more consistent with $\tau_{\text{d}} \propto M_{\text{BH}}^{0.65 \pm 0.01} \lambda_{\text{Edd}}^{0.65 \pm 0.01}$ (Zhou et al. 2024), predicted by the corona heated accretion disc reprocessing model (Sun et al. 2020b,a), which takes the time-dependent evolution of the standard thin disk into account.

Additionally, it is interesting to note that Montano et al. (2022) reported a $\tau_{\text{gz}} - M_{\text{BH}}$ relation with a similar mass index of $0.63_{-0.21}^{+0.16}$, where τ_{gz} is the time delay of the z -band variation relative to the g -band one. Although the lag τ_{gz} is very different from the timescales of SFs we discussed here, the similar mass index may also suggest that they have the same physical origin. Nonetheless, we caution that the $\tau_{\text{gz}} - M_{\text{BH}}$ relation could be subject to the same selection bias affecting the lag-luminosity relation, as discussed recently by Chen et al. (2024).

3.2. Color Variation (CV)

3.2.1. Plausible timescale-dependent CVs at the intermediate-mass scale

Adopting the 3σ -cut variation significance and within the proper ranges of timescales for any two bands, Figure 11 shows in the flux space the CVs for NGC 4395 monitored in three nights: the FNT-1 (filled circles), the FNT-2 (open squares), and the GTC night (open triangles). The CVs vary much in the three nights of observation. The FNT-1 CVs based on the FNT-1 light curves span a widest range of timescale and the timescale dependency seems to be the most significant. Although the FNT-2 CVs based on the FNT-2 light curves span a narrower range of timescale than the FNT-1 CVs, a nicely consistency between them can be found in several band pairs (e.g., $r - z$ and $i - z$), while a combination of

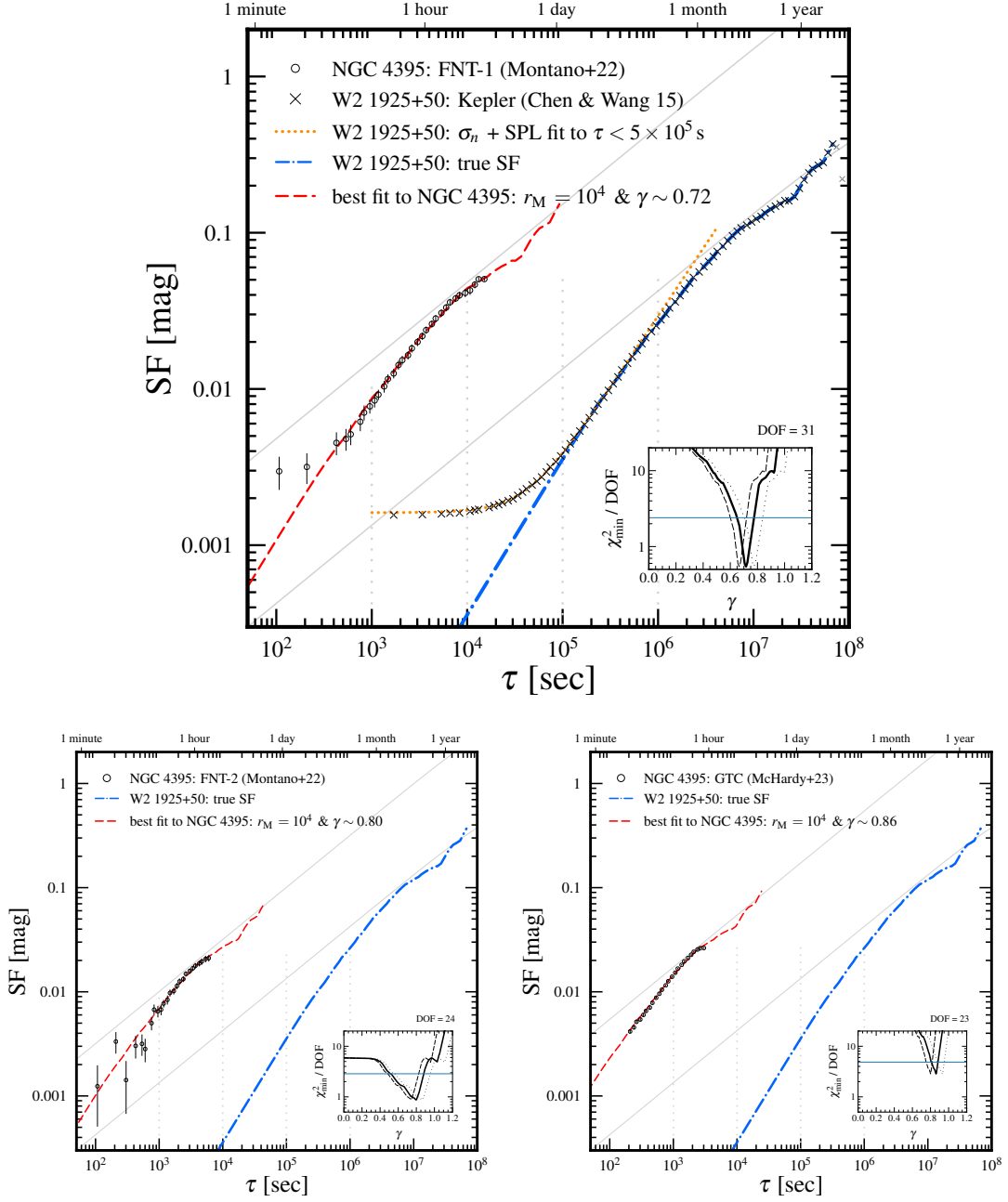


Figure 7. Same as Figure 6, but for comparing NGC 4395 ($M_{\text{BH}} \simeq 10^4 M_{\odot}$) with W2 1925+50 ($M_{\text{BH}} \simeq 10^8 M_{\odot}$) and $r_{\text{M}} = 10^4$. The observed SF of W2 1925+50 (crosses) is derived from the *Kepler* light curves stitched by [Chen & Wang \(2015\)](#). The σ_n + SPL fit is limited to $\tau \lesssim 5 \times 10^5$ s.

them may suggest a clearer timescale dependence (e.g., $g-r$ and $g-i$). Owing to the short baseline of the GTC light curves and the large GTC z -band photometric uncertainty (Table 1), there is no remaining data point for the GTC CVs involving the z band and the GTC CVs are globally less reliable.

Since the FNT-1 CVs span the widest range of timescale and show a potential timescale dependence, we present a quantitative discussion on the

timescale dependency of the FNT-1 CVs. We employ a linear least-squares regression fitting package `scipy.stats.linregress` ([Virtanen et al. 2020](#)) to assess the significance of the timescale dependency with a smaller p -value indicating a more significant departure from a zero slope (i.e., no timescale dependence). As depicted in the diagonal sub-panels of Figure 11, we confirm significant timescale-dependent CVs in the band pairs involving z band. The p -values are 0.04, 0.03, and

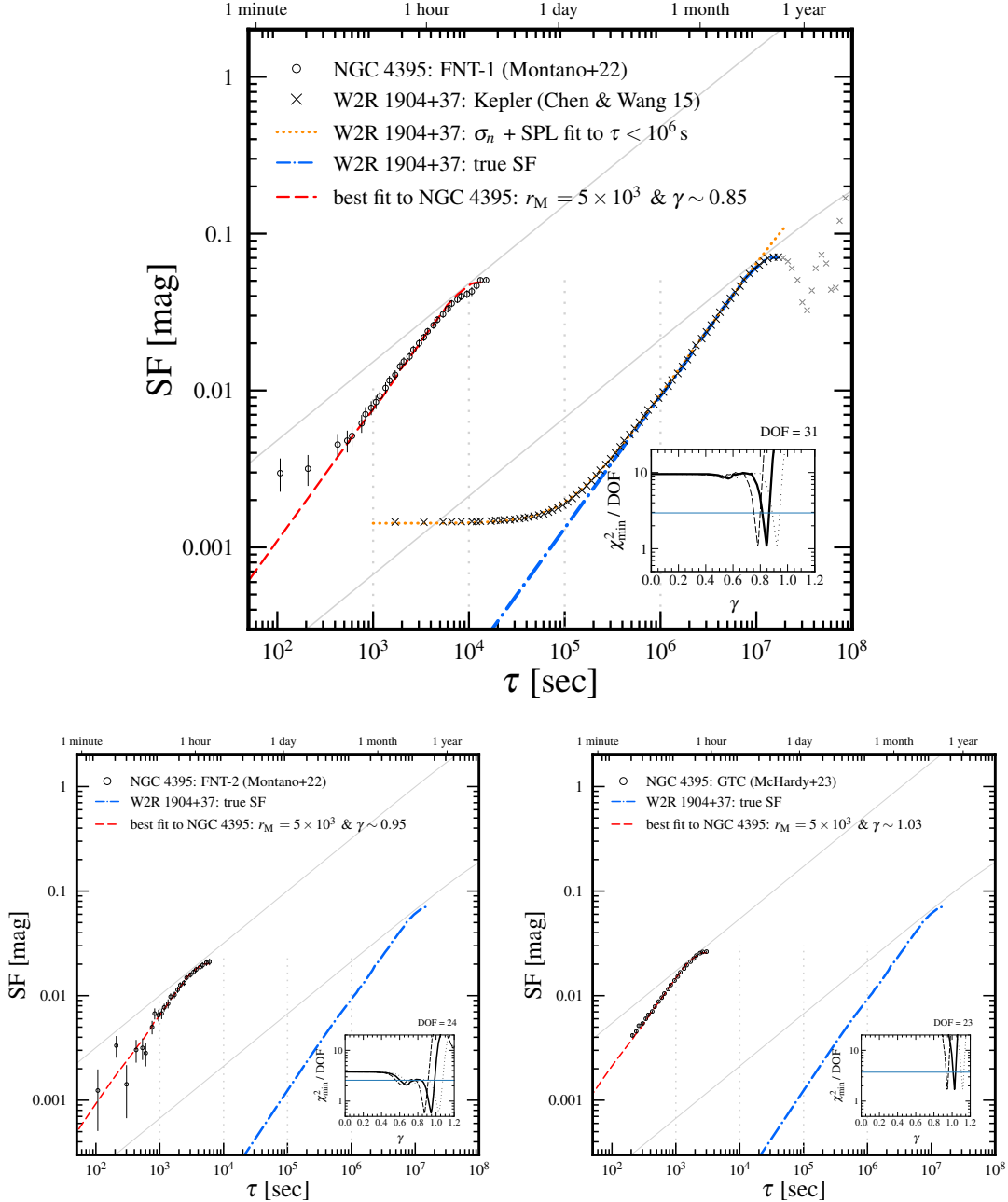


Figure 8. Same as Figure 6, but for comparing NGC 4395 ($M_{\text{BH}} \simeq 10^4 M_{\odot}$) with W2R 1904+37 ($M_{\text{BH}} \simeq 5 \times 10^7 M_{\odot}$) and $r_{\text{M}} = 5 \times 10^3$. The observed SF of W2R 1904+37 (crosses) is derived from the *Kepler* light curves stitched by [Chen & Wang \(2015\)](#). The σ_n + SPL fit is limited to $\tau \lesssim 10^6$ s.

0.01 for the g - z , r - z , and i - z band pairs, respectively. For the other band pairs (i.e., g - r , g - i , and r - i), we notice that these CVs decrease with increasing timescales up to ~ 5000 s (hereafter, a declining trend), and the prominence of the global timescale dependency is reduced, with p -values of 0.41, 0.47, and 0.90 for the g - r , g - i , and r - i band pairs, respectively.

The CV approximately measures the ratio of SFs between two bands, and thus is more easily affected by

poorer observational conditions and the randomness nature of AGN variability. First, the importance of the the baseline and photometric uncertainties of light curves is suggested by a coincidence: the most prominent CVs of NGC 4395 are revealed by the longest FNT-1 light curves. Second, the effect of the randomness nature of AGN variability is demonstrated by another coincidence: clearer timescale-dependent CVs of NGC 4395

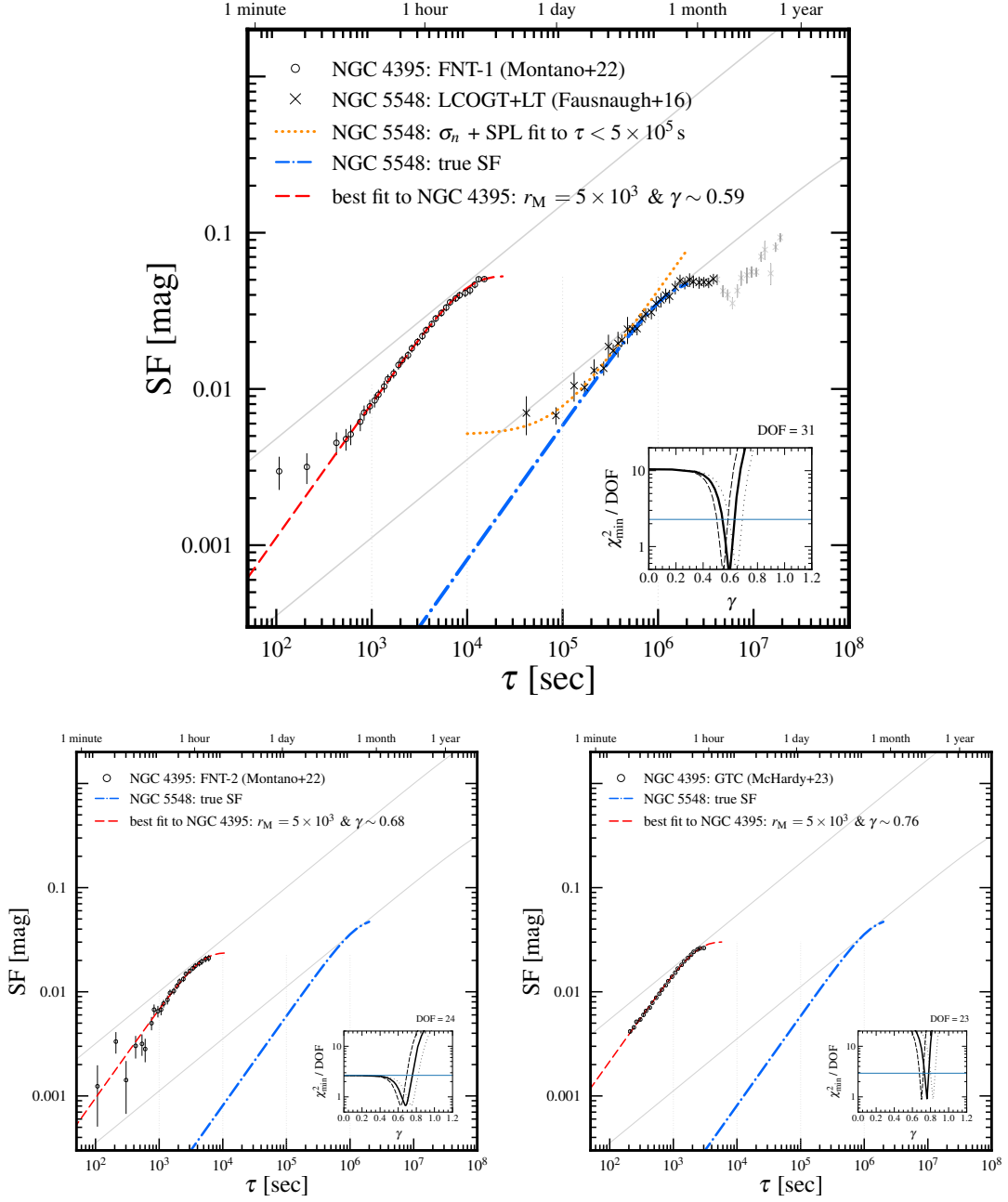


Figure 9. Same as Figure 6, but for comparing NGC 4395 ($M_{\text{BH}} \simeq 10^4 M_{\odot}$) with NGC 5548 ($M_{\text{BH}} \simeq 5 \times 10^7 M_{\odot}$) and $r_M = 5 \times 10^3$. The observed SF of NGC 5548 (crosses) is derived from the *i*-band light curve of Fausnaugh et al. (2016). The σ_n + SPL fit is limited to $\tau \lesssim 5 \times 10^5$ s.

(Figure 11) correspond to more significant variations with larger $\sigma_{\text{rms}}/\sigma_e$ (the right panel of Figure 3).

Besides, the contribution of the broad Balmer line can also reduce the timescale dependency. We notice that there are broad H α and H β lines located in the *r* and *g* bands, respectively. The variation of the broad H α line likely lags that of the *V*-band continuum by $\sim 50 - 100$ min (Woo et al. 2019; Cho et al. 2020, 2021), just corresponding to timescales of ~ 3000 s to ~ 6000 s.

Being guided by simulations of Zhu et al. (2018, cf. their Figure 3), besides the photometric uncertainty, the delayed H α (H β) variation in the *r* (*g*) band can also contribute to the declining trend involved in the *r* (*g*) versus *i* CV. For the FNT-1 CVs of NGC 4395, if we exclude data points at timescales $\lesssim 5000$ s, very clear monotonic CVs are found for all band pairs.

At any timescale, the CV always behaves BWB, except for the *r* versus *i* case (and somewhat the *r* ver-

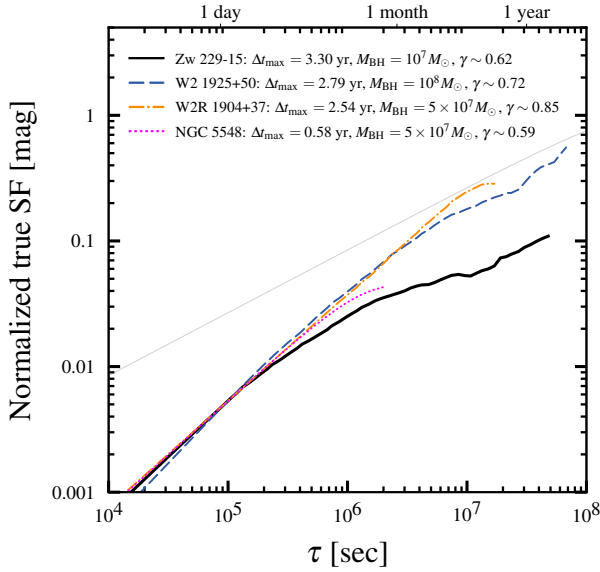


Figure 10. The true SFs of four AGNs at the supermassive scale, i.e., Zw 229-15 (solid curve), W2 1925+50 (dashed curve), W2R 1904+37 (dot-dashed curve), and NGC 5548 (dotted curve), are taken from Figures 6 to 9, and normalized to that of Zw 229-15 at $\tau = 10^5$ s. For the three *Kepler* AGNs, the SF of Zw 229-15 flattens first, followed by W2 1925+50 and W2R 1904+37. The BH mass of W2R 1904+37 intervenes between Zw 229-15 and W2 1925+50, however, its SF likely flattens at the longest timescale, indicating that its true BH mass may be larger than measured by Smith et al. (2018). The baselines of Zw 229-15 and W2 1925+50 are the longest, and the resultant γ are also comparable. For NGC 5548, its baseline is too short, i.e., only 0.58 yr, to reach any firm conclusion on γ .

such z case), where RWB trends are found in all three nights. The RWB trend is just attributed to the fact that the r -band variation amplitudes are smaller than the i -band ones (the left panel of Figure 3), contrary to the general declining variation amplitude with increasing wavelength for AGNs. Although there is contribution of broad $H\alpha$ emission line in the r band (Figure 1), the exact reason for the smaller r -band variation amplitude is unclear.

In short, using the current available data, we can only show plausible timescale-dependent CVs for NGC 4395 at the intermediate-mass scale. Longer and repeated observations on NGC 4395 are essential for confirmation.

3.2.2. Comparing CVs of AGNs across the intermediate-mass to supermassive scales

Utilizing high-cadence (~ 1 -3 days), long-baseline (~ 450 days) *Swift* light curves in six UV/optical bands (i.e., UVW2, UVM2, UVW1, U, B, and V), Zhu et al. (2018) investigated the timescale dependency of CVs for NGC 5548. They revealed the timescale-dependent

CVs in NGC 5548 at the supermassive scale for the first time. Taking the plausible timescale-dependent CVs for NGC 4395 at the intermediate-mass scale reported in Section 3.2.1, we now have a unique opportunity to compare the CVs across different mass scales. Before such a comparison, we first check the CVs for NGC 5548 in band pairs longer than those considered by Zhu et al. (2018).

We notice that the *griz*-band light curves of NGC 5548 were obtained with ground-based telescopes only. These light curves published by Fausnaugh et al. (2016) span a baseline of ~ 180 days much shorter than those of *Swift* used by Zhu et al. (2018). Following Zhu et al. (2018), these light curves are binned with bin sizes of 0.5 days. After that, we calculate the CVs in the flux space following the methodology outlined in Section 2.3. The resultant CVs for NGC 5548 across the *griz* bands are depicted in Figure 11 as open asterisks with the top gray axes. According to the linear regression analysis, the CVs of NGC 5548 involving g - i and r - i band pairs exhibit significant timescale dependency with positive slopes and p -values of 0.03 and 0.04, respectively. While for the g - r , g - z , and r - z band pairs, the significance are low with p -values of 0.81, 0.53, and 0.52, respectively. For the i - z band, a negative slope is even found with a p -value of 0.31.

Shortening the light curves of NGC 5548 from ~ 450 days to ~ 180 days, we confirm that the CVs of the *Swift* band pairs are nearly the same as reported by Zhu et al. (2018), except at the longest timescales around ~ 100 days where values of the CVs of almost all *Swift* band pairs become much smaller (i.e., behaving as a declining trend) for the shortened *Swift* light curves. This fact may suggest that for the r - i , r - z , and i - z band pairs the declining trends around $\sim 2 \times 10^6$ s found in Figure 11 are likely due to the limited baseline. Therefore, much longer and regular monitoring on NGC 5548 at optical wavelengths is necessary before claiming the timescale dependency of the CVs between optical bands.

Nevertheless, we make a tentative comparison on the CVs between NGC 5548 and NGC 4395. Assuming $\gamma = 0.6$ (Section 3.1.3), we horizontally scale the CVs of NGC 5548 by a factor of r_M^γ where $r_M = 5000$. The scaled CVs of NGC 5548 (represented by open asterisks with the bottom black axes) are depicted in Figure 11, revealing a similar dynamical range of timescales showing the timescale dependency for both NGC 5548 and NGC 4395. In the future, with longer light curves we can better measure the CVs for AGNs across different mass scales and could use them to directly compare and constrain the mass index γ .

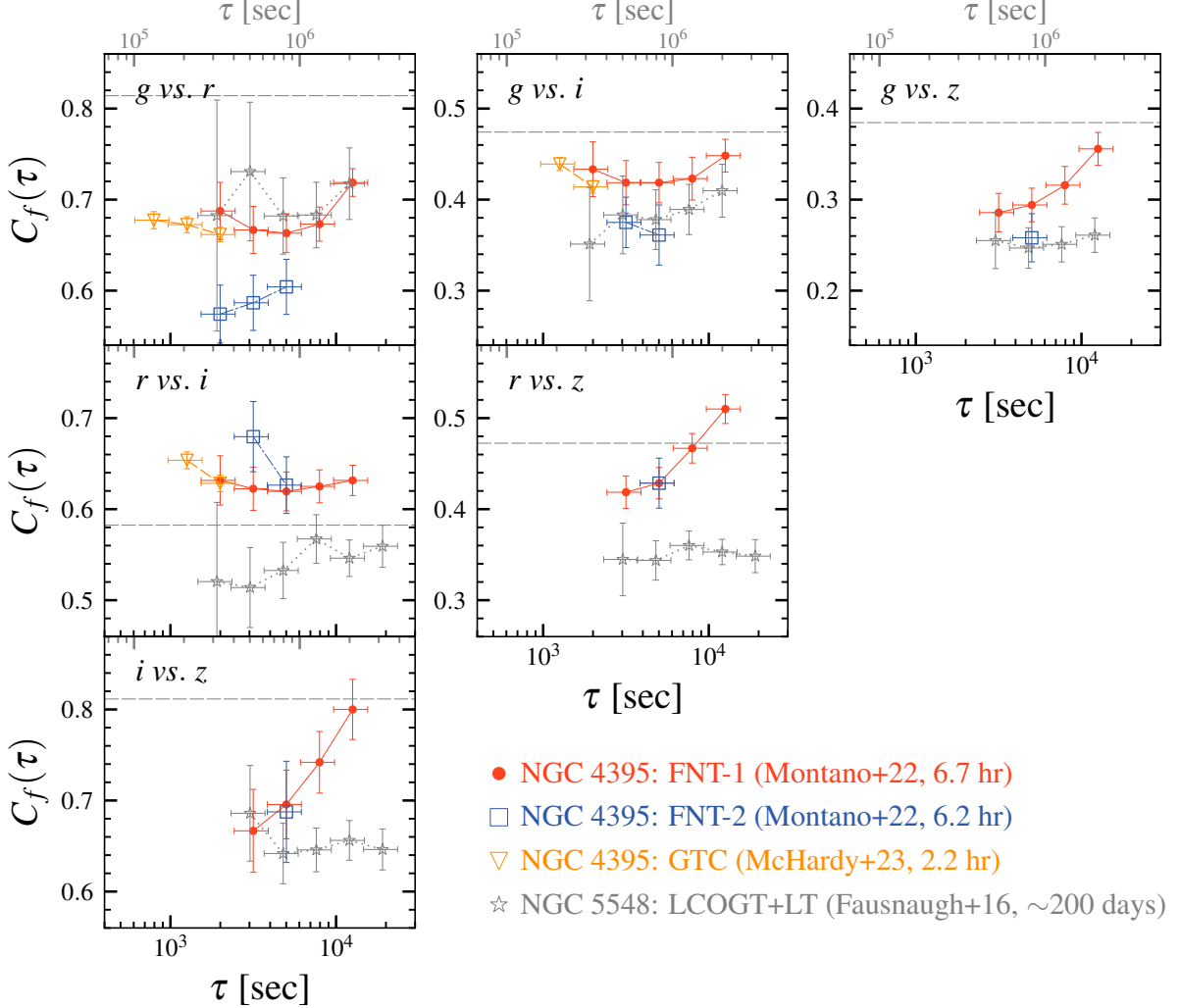


Figure 11. Comparison on the CVs in the flux space between *griz* bands for AGNs across the intermediate-mass (NGC 4395 with $M_{\text{BH}} \simeq 10^4 M_{\odot}$) to supermassive (NGC 5548 with $M_{\text{BH}} \simeq 5 \times 10^7 M_{\odot}$) scales. For NGC 4395, shown are CVs in their nights: the FNT-1 (Montano et al. 2022, filled circles), the FNT-2 (Montano et al. 2022, open squares), and the GTC night (McHardy et al. 2023, open triangles). For NGC 5548, the *griz*-band light curves of Fausnaugh et al. (2016) are used to derive the CVs (open asterisks with the top gray axes), timescales of which are scaled down by a factor of r_M^γ with $r_M = 5000$ and $\gamma = 0.6$ (open asterisks with the bottom black axes). In each panel, the gray dashed horizontal line indicates the mean flux ratio of the redder band to the bluer one over three nights, \bar{f}^r/\bar{f}^b , below (above) which AGNs behave bluer (redder) when brightening. Note that shown are only those data points within the proper range of timescales deemed to be less affected by both the photometric uncertainty and limited baseline (Figure 5). The y -axis of all panels has the same relative dynamical range.

3.3. New evidence against the traditional reprocessing scenario but for the thermal fluctuation scenario?

By analyzing multi-band light curves of NGC 4395, all studies (Desroches et al. 2006; McHardy et al. 2016; Montano et al. 2022; McHardy et al. 2023) had merely focused on its lag-wavelength relation, claiming either a consistency with or a departure from the prediction by the Shakura & Sunyaev (1973) disk (SSD; Figure 12). The diverse lag-wavelength relations measured in different nights for NGC 4395 had been interpreted dif-

ferently: randomness of thermal fluctuation (Cai et al. 2020; Z. B. Su et al. 2024a, in preparation), contamination of the diffuse continuum emission from the broad-line region (Montano et al. 2022), or the imprint of the outer edge of the accretion disk (McHardy et al. 2023).

Here, we propose the diverse lag-wavelength relations for NGC 4395 (Figure 12) as a potential new evidence against the traditional reprocessing scenario, which implies very stable lags (Sun et al. 2019, cf. their Figure 3) and cannot explain the large and significant difference

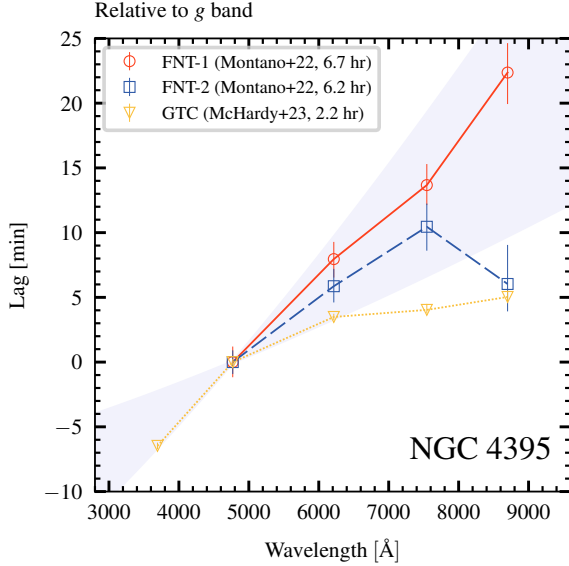


Figure 12. Three distinct lag-wavelength relations for NGC 4395 measured in three nights by McHardy et al. (2023, 2.2 hr) and Montano et al. (2022, 6.7 hr for the FNT-1 and 6.2 hr for the FNT-2) plausibly indicate the randomness of lag implied by the disk thermal fluctuation (Cai et al. 2018, 2020). The time lags are relative to the g band. The shaded region is enclosed by two SSD-predicted lag-wavelength relations calculated following Equation (12) of Fausnaugh et al. (2016) with the radiation efficiency $\eta = 0.1$, the ratio of external to internal heating $\kappa = 1$, the conversion factor of temperature to wavelength $X = 5.04$ (Tie & Kochanek 2018), the bolometric luminosity of 5.3×10^{40} erg s $^{-1}$ (Moran et al. 2005), and two distinct BH masses of $1.7 \times 10^4 M_{\odot}$ (Cho et al. 2021) and $4 \times 10^5 M_{\odot}$ (den Brok et al. 2015).

in lags among nights. In Figure 12, for the r , i , and z bands relative to the g band, the ratios of lags measured by Montano et al. (2022, the Night-1) and those by McHardy et al. (2023) are as large as $\simeq 2.2$, $\simeq 3.3$, and $\simeq 4.2$ with confidence levels reaching $\simeq 3.2\sigma$, $\simeq 5.8\sigma$, and $\simeq 7.0\sigma$, respectively. Admittedly, the mean fluxes of McHardy et al. (2023) are lower than those of Montano et al. (2022) by a factor of $\simeq 1.14$ on average (Figure 2). According to the lag-luminosity relation, i.e., $\tau_{\text{lag}} \propto L^{0.5}$ (Sergeev et al. 2005), the smaller flux by a factor of $\simeq 1.14$ corresponds to a smaller lag by a factor of $\simeq 1.07$, which is too small to account for the large difference in the observed lags.

Instead, a large difference in lags as a result of the randomness of disk fluctuation has been predicted by the simple thermal fluctuation scenario (Cai et al. 2018, 2020; Z. B. Su et al., 2024a, in preparation) and thermal fluctuations induced by corona heating through magnetic field (Sun et al. 2020b,a; Sun 2023). More quantitative comparisons between the models (both the

thermal fluctuation model and the reprocessing model) and the data (both the lag-wavelength relation and the timescale-dependent CV) are being conducted for NGC 4395 (Z. B. Su et al. 2024c, in preparation) after we have upgraded the radiation efficiency for general AGNs, including NGC 4395 (briefly, its η is likely as small as ~ 0.001 rather than the commonly assumed 0.1; Z. B. Su et al. 2024b, in preparation).

4. SUMMARY

In this work, we analyze three nights of *griz*-band light curves of NGC 4395. At the intermediate-mass scale, we unveil for the first time prominent departures from the DRW process at timescales shorter than \sim hours in all three nights and four bands of observation on NGC 4395. Additionally, we can only show plausible timescale-dependent CVs for NGC 4395 in the longest two nights of observation.

By comparing optical variations, i.e., the SFs, across the intermediate-mass (NGC 4395) to supermassive (mainly Zw 229-15 and W2 1925+50) scales, we suggest a new scaling relation between the optical variation timescale and BH mass with a mass slope of $\simeq 0.6 - 0.8$. This mass index differs from most previous measurements but is consistent with a recent theoretical prediction by the time-dependent evolution of the standard thin disk, suggesting a similar accretion process and variability in AGNs across various mass scales.

In near future, many facilities, such as the Multi-channel Imager onboard the Chinese Space Station Telescope (Zhan 2021), the Multi-channel Photometric Survey telescope (Mephisto; e.g., Liu 2019; Lei et al. 2021), and the Wide Field Survey Telescope (Wang et al. 2023) will be extremely helpful in exploring the AGN variability, including the SF, CV, and lag-wavelength relation.

ACKNOWLEDGEMENT

We are grateful to the anonymous referee for many constructive comments, to Ian McHardy for sharing and clarifying the light curves of NGC 4395, and to Xue-Bing Wu for helpful comments. This work is supported by National Key R&D Program of China (grant No. 2023YFA1607903) and the National Science Foundation of China (grant Nos. 12373016 and 12033006). Z.Y.C. acknowledges support from the science research grants from the China Manned Space Project under grant no. CMS-CSST-2021-A06 and the Cyrus Chun Ying Tang Foundations. M.Y.S. acknowledges support from the National Natural Science Foundation of China (NSFC-12322303) and the Natural Science Foundation of Fujian Province of China (No. 2022J06002).

Software: `julia` Programming Language (Bezanson et al. 2017), `UncertainData.jl` (Haaga 2019), `Numpy`

(Harris et al. 2020), `Scipy` (Virtanen et al. 2020), `Matplotlib` (Hunter 2007).

REFERENCES

- Andrae, R., Kim, D. W., & Bailer-Jones, C. A. L. 2013, *A&A*, 554, A137, doi: [10.1051/0004-6361/201321335](https://doi.org/10.1051/0004-6361/201321335)
- Arévalo, P., Churazov, E., Lira, P., et al. 2023a, arXiv e-prints, arXiv:2306.11099, doi: [10.48550/arXiv.2306.11099](https://doi.org/10.48550/arXiv.2306.11099)
- Arévalo, P., Churazov, E., Zhuravleva, I., Hernández-Monteagudo, C., & Revnivtsev, M. 2012, *MNRAS*, 426, 1793, doi: [10.1111/j.1365-2966.2012.21789.x](https://doi.org/10.1111/j.1365-2966.2012.21789.x)
- Arévalo, P., Lira, P., Sánchez-Sáez, P., et al. 2023b, *MNRAS*, 526, 6078, doi: [10.1093/mnras/stad3186](https://doi.org/10.1093/mnras/stad3186)
- Barth, A. J., Nguyen, M. L., Malkan, M. A., et al. 2011, *ApJ*, 732, 121, doi: [10.1088/0004-637X/732/2/121](https://doi.org/10.1088/0004-637X/732/2/121)
- Bessell, M. S. 2005, *ARA&A*, 43, 293, doi: [10.1146/annurev.astro.41.082801.100251](https://doi.org/10.1146/annurev.astro.41.082801.100251)
- Bezanson, J., Edelman, A., Karpinski, S., & Shah, V. B. 2017, *SIAM Review*, 59, 65, doi: [10.1137/141000671](https://doi.org/10.1137/141000671)
- Burke, C. J., Shen, Y., Chen, Y.-C., et al. 2020, *ApJ*, 899, 136, doi: [10.3847/1538-4357/aba3ce](https://doi.org/10.3847/1538-4357/aba3ce)
- Burke, C. J., Shen, Y., Blaes, O., et al. 2021, *Science*, 373, 789, doi: [10.1126/science.abg9933](https://doi.org/10.1126/science.abg9933)
- Cai, Z., Sun, Y., Wang, J., et al. 2019, *Science China Physics, Mechanics, and Astronomy*, 62, 69511, doi: [10.1007/s11433-018-9330-4](https://doi.org/10.1007/s11433-018-9330-4)
- Cai, Z.-Y., Wang, J.-X., Gu, W.-M., et al. 2016, *ApJ*, 826, 7, doi: [10.3847/0004-637X/826/1/7](https://doi.org/10.3847/0004-637X/826/1/7)
- Cai, Z.-Y., Wang, J.-X., & Sun, M. 2020, *ApJ*, 892, 63, doi: [10.3847/1538-4357/ab7991](https://doi.org/10.3847/1538-4357/ab7991)
- Cai, Z.-Y., Wang, J.-X., Zhu, F.-F., et al. 2018, *ApJ*, 855, 117, doi: [10.3847/1538-4357/aab091](https://doi.org/10.3847/1538-4357/aab091)
- Caplar, N., Lilly, S. J., & Trakhtenbrot, B. 2017, *ApJ*, 834, 111, doi: [10.3847/1538-4357/834/2/111](https://doi.org/10.3847/1538-4357/834/2/111)
- Chen, J., Sun, M., & Zhang, Z.-X. 2024, *ApJ*, 962, 134, doi: [10.3847/1538-4357/ad16ea](https://doi.org/10.3847/1538-4357/ad16ea)
- Chen, X.-Y., & Wang, J.-X. 2015, *ApJ*, 805, 80, doi: [10.1088/0004-637X/805/1/80](https://doi.org/10.1088/0004-637X/805/1/80)
- Cho, H., Woo, J.-H., Hodges-Kluck, E., et al. 2020, *ApJ*, 892, 93, doi: [10.3847/1538-4357/ab7a98](https://doi.org/10.3847/1538-4357/ab7a98)
- Cho, H., Woo, J.-H., Treu, T., et al. 2021, *ApJ*, 921, 98, doi: [10.3847/1538-4357/ac1e92](https://doi.org/10.3847/1538-4357/ac1e92)
- Cutri, R. M., Wisniewski, W. Z., Rieke, G. H., & Lebofsky, M. J. 1985, *ApJ*, 296, 423, doi: [10.1086/163461](https://doi.org/10.1086/163461)
- den Brok, M., Seth, A. C., Barth, A. J., et al. 2015, *ApJ*, 809, 101, doi: [10.1088/0004-637X/809/1/101](https://doi.org/10.1088/0004-637X/809/1/101)
- Denney, K. D., Watson, L. C., Peterson, B. M., et al. 2009, *ApJ*, 702, 1353, doi: [10.1088/0004-637X/702/2/1353](https://doi.org/10.1088/0004-637X/702/2/1353)
- Desroches, L.-B., Filippenko, A. V., Kaspi, S., et al. 2006, *ApJ*, 650, 88, doi: [10.1086/507263](https://doi.org/10.1086/507263)
- Dexter, J., & Agol, E. 2011, *ApJL*, 727, L24, doi: [10.1088/2041-8205/727/1/L24](https://doi.org/10.1088/2041-8205/727/1/L24)
- di Clemente, A., Giallongo, E., Natali, G., Trevese, D., & Vagnetti, F. 1996, *ApJ*, 463, 466, doi: [10.1086/177261](https://doi.org/10.1086/177261)
- Emmanoulopoulos, D., McHardy, I. M., & Uttley, P. 2010, *MNRAS*, 404, 931, doi: [10.1111/j.1365-2966.2010.16328.x](https://doi.org/10.1111/j.1365-2966.2010.16328.x)
- Fausnaugh, M. M., Denney, K. D., Barth, A. J., et al. 2016, *ApJ*, 821, 56, doi: [10.3847/0004-637X/821/1/56](https://doi.org/10.3847/0004-637X/821/1/56)
- Filippenko, A. V., & Ho, L. C. 2003, *ApJL*, 588, L13, doi: [10.1086/375361](https://doi.org/10.1086/375361)
- Filippenko, A. V., & Sargent, W. L. W. 1989, *ApJL*, 342, L11, doi: [10.1086/185472](https://doi.org/10.1086/185472)
- Guo, H., & Gu, M. 2016, *ApJ*, 822, 26, doi: [10.3847/0004-637X/822/1/26](https://doi.org/10.3847/0004-637X/822/1/26)
- Guo, H., Wang, J., Cai, Z., & Sun, M. 2017, *ApJ*, 847, 132, doi: [10.3847/1538-4357/aa8d71](https://doi.org/10.3847/1538-4357/aa8d71)
- Haaga, K. A. 2019, *Journal of Open Source Software*, 4, 1666, doi: [10.21105/joss.01666](https://doi.org/10.21105/joss.01666)
- Harris, C. R., Millman, K. J., van der Walt, S. J., et al. 2020, *Nature*, 585, 357, doi: [10.1038/s41586-020-2649-2](https://doi.org/10.1038/s41586-020-2649-2)
- Hu, X.-F., Cai, Z.-Y., & Wang, J.-X. 2023, arXiv e-prints, arXiv:2310.16223, doi: [10.48550/arXiv.2310.16223](https://doi.org/10.48550/arXiv.2310.16223)
- Hunter, J. D. 2007, *Computing in Science & Engineering*, 9, 90, doi: [10.1109/MCSE.2007.55](https://doi.org/10.1109/MCSE.2007.55)
- Kasliwal, V. P., Vogeley, M. S., & Richards, G. T. 2015, *MNRAS*, 451, 4328, doi: [10.1093/mnras/stv1230](https://doi.org/10.1093/mnras/stv1230)
- Kelly, B. C., Bechtold, J., & Siemiginowska, A. 2009, *ApJ*, 698, 895, doi: [10.1088/0004-637X/698/1/895](https://doi.org/10.1088/0004-637X/698/1/895)
- Kelly, B. C., Becker, A. C., Sobolewska, M., Siemiginowska, A., & Uttley, P. 2014, *ApJ*, 788, 33, doi: [10.1088/0004-637X/788/1/33](https://doi.org/10.1088/0004-637X/788/1/33)
- Koch, D. G., Borucki, W. J., Basri, G., et al. 2010, *ApJL*, 713, L79, doi: [10.1088/2041-8205/713/2/L79](https://doi.org/10.1088/2041-8205/713/2/L79)
- Kozłowski, S. 2016, *ApJ*, 826, 118, doi: [10.3847/0004-637X/826/2/118](https://doi.org/10.3847/0004-637X/826/2/118)
- Kozłowski, S., Kochanek, C. S., Udalski, A., et al. 2010, *ApJ*, 708, 927, doi: [10.1088/0004-637X/708/2/927](https://doi.org/10.1088/0004-637X/708/2/927)
- Lei, L., Li, J. D., Wu, J. T., Jiang, S. Y., & Chen, B. Q. 2021, *Astronomical Research & Technology*, 18, 115121, doi: [10.14005/j.cnki.issn1672-7673.20200713.001](https://doi.org/10.14005/j.cnki.issn1672-7673.20200713.001)
- Liu, X. 2019, in *Galactic Archaeology in the Gaia Era*, 14

- MacLeod, C. L., Ivezić, Ž., Kochanek, C. S., et al. 2010, *ApJ*, 721, 1014, doi: [10.1088/0004-637X/721/2/1014](https://doi.org/10.1088/0004-637X/721/2/1014)
- McHardy, I. M., Connolly, S. D., Peterson, B. M., et al. 2016, *Astronomische Nachrichten*, 337, 500, doi: [10.1002/asna.201612337](https://doi.org/10.1002/asna.201612337)
- McHardy, I. M., Beard, M., Breedt, E., et al. 2023, *MNRAS*, 519, 3366, doi: [10.1093/mnras/stac3651](https://doi.org/10.1093/mnras/stac3651)
- Montano, J. W., Guo, H., Barth, A. J., et al. 2022, *ApJL*, 934, L37, doi: [10.3847/2041-8213/ac7e54](https://doi.org/10.3847/2041-8213/ac7e54)
- Moran, E. C., Eracleous, M., Leighly, K. M., et al. 2005, *AJ*, 129, 2108, doi: [10.1086/429522](https://doi.org/10.1086/429522)
- Mushotzky, R. F., Edelson, R., Baumgartner, W., & Gandhi, P. 2011, *ApJL*, 743, L12, doi: [10.1088/2041-8205/743/1/L12](https://doi.org/10.1088/2041-8205/743/1/L12)
- Pancoast, A., Brewer, B. J., Treu, T., et al. 2014, *MNRAS*, 445, 3073, doi: [10.1093/mnras/stu1419](https://doi.org/10.1093/mnras/stu1419)
- Peterson, B. M., Bentz, M. C., Desroches, L.-B., et al. 2005, *ApJ*, 632, 799, doi: [10.1086/444494](https://doi.org/10.1086/444494)
- Reynolds, C. S., & Miller, M. C. 2009, *ApJ*, 692, 869, doi: [10.1088/0004-637X/692/1/869](https://doi.org/10.1088/0004-637X/692/1/869)
- Ricker, G. R., Winn, J. N., Vanderpek, R., et al. 2015, *Journal of Astronomical Telescopes, Instruments, and Systems*, 1, 014003, doi: [10.1117/1.JATIS.1.1.014003](https://doi.org/10.1117/1.JATIS.1.1.014003)
- Ruan, J. J., Anderson, S. F., Dexter, J., & Agol, E. 2014, *ApJ*, 783, 105, doi: [10.1088/0004-637X/783/2/105](https://doi.org/10.1088/0004-637X/783/2/105)
- Schmidt, K. B., Rix, H.-W., Shields, J. C., et al. 2012, *ApJ*, 744, 147, doi: [10.1088/0004-637X/744/2/147](https://doi.org/10.1088/0004-637X/744/2/147)
- Sergeev, S. G., Doroshenko, V. T., Golubinskiy, Y. V., Merkulova, N. I., & Sergeeva, E. A. 2005, *ApJ*, 622, 129, doi: [10.1086/427820](https://doi.org/10.1086/427820)
- Shakura, N. I., & Sunyaev, R. A. 1973, *A&A*, 24, 337
- Simm, T., Salvato, M., Saglia, R., et al. 2016, *A&A*, 585, A129, doi: [10.1051/0004-6361/201527353](https://doi.org/10.1051/0004-6361/201527353)
- Smith, K. L., Mushotzky, R. F., Boyd, P. T., et al. 2018, *ApJ*, 857, 141, doi: [10.3847/1538-4357/aab88d](https://doi.org/10.3847/1538-4357/aab88d)
- Stone, Z., Shen, Y., Burke, C. J., et al. 2023, *MNRAS*, 521, 836, doi: [10.1093/mnras/stad592](https://doi.org/10.1093/mnras/stad592)
- Suberlak, K. L., Ivezić, Ž., & MacLeod, C. 2021, *ApJ*, 907, 96, doi: [10.3847/1538-4357/abc698](https://doi.org/10.3847/1538-4357/abc698)
- Sun, M. 2023, *MNRAS*, 521, 2954, doi: [10.1093/mnras/stad740](https://doi.org/10.1093/mnras/stad740)
- Sun, M., Xue, Y., Trump, J. R., & Gu, W.-M. 2019, *MNRAS*, 482, 2788, doi: [10.1093/mnras/sty2885](https://doi.org/10.1093/mnras/sty2885)
- Sun, M., Xue, Y., Wang, J., Cai, Z., & Guo, H. 2018, *ApJ*, 866, 74, doi: [10.3847/1538-4357/aae208](https://doi.org/10.3847/1538-4357/aae208)
- Sun, M., Xue, Y., Guo, H., et al. 2020a, *ApJ*, 902, 7, doi: [10.3847/1538-4357/abb1c4](https://doi.org/10.3847/1538-4357/abb1c4)
- Sun, M., Xue, Y., Brandt, W. N., et al. 2020b, *ApJ*, 891, 178, doi: [10.3847/1538-4357/ab789e](https://doi.org/10.3847/1538-4357/ab789e)
- Sun, Y.-H., Wang, J.-X., Chen, X.-Y., & Zheng, Z.-Y. 2014, *ApJ*, 792, 54, doi: [10.1088/0004-637X/792/1/54](https://doi.org/10.1088/0004-637X/792/1/54)
- Tang, J.-J., Wolf, C., & Tonry, J. 2023, *Nature Astronomy*, 7, 473, doi: [10.1038/s41550-022-01885-8](https://doi.org/10.1038/s41550-022-01885-8)
- Tie, S. S., & Kochanek, C. S. 2018, *MNRAS*, 473, 80, doi: [10.1093/mnras/stx2348](https://doi.org/10.1093/mnras/stx2348)
- Vaughan, S., Edelson, R., Warwick, R. S., & Uttley, P. 2003, *MNRAS*, 345, 1271, doi: [10.1046/j.1365-2966.2003.07042.x](https://doi.org/10.1046/j.1365-2966.2003.07042.x)
- Virtanen, P., Gommers, R., Oliphant, T. E., et al. 2020, *Nature Methods*, 17, 261, doi: [10.1038/s41592-019-0686-2](https://doi.org/10.1038/s41592-019-0686-2)
- Wall, J. V., & Jenkins, C. R. 2012, *Practical Statistics for Astronomers* (Cambridge University Press)
- Wang, T., Liu, G., Cai, Z., et al. 2023, *Science China Physics, Mechanics, and Astronomy*, 66, 109512, doi: [10.1007/s11433-023-2197-5](https://doi.org/10.1007/s11433-023-2197-5)
- Woo, J.-H., Cho, H., Gallo, E., et al. 2019, *Nature Astronomy*, 3, 755, doi: [10.1038/s41550-019-0790-3](https://doi.org/10.1038/s41550-019-0790-3)
- Wu, Y.-J., Wang, J.-X., Cai, Z.-Y., et al. 2020, *Science China Physics, Mechanics, and Astronomy*, 63, 129512, doi: [10.1007/s11433-020-1611-7](https://doi.org/10.1007/s11433-020-1611-7)
- Zhan, H. 2021, *Chinese Science Bulletin*, 66, 1290
- Zhou, S., Sun, M., Cai, Z.-Y., et al. 2024, arXiv e-prints, arXiv:2403.01691. <https://arxiv.org/abs/2403.01691>
- Zhu, F.-F., Wang, J.-X., Cai, Z.-Y., & Sun, Y.-H. 2016, *ApJ*, 832, 75, doi: [10.3847/0004-637X/832/1/75](https://doi.org/10.3847/0004-637X/832/1/75)
- Zhu, F.-F., Wang, J.-X., Cai, Z.-Y., et al. 2018, *apj*, 860, 29, doi: [10.3847/1538-4357/aac2d7](https://doi.org/10.3847/1538-4357/aac2d7)
- Zu, Y., Kochanek, C. S., Kozłowski, S., & Udalski, A. 2013a, *ApJ*, 765, 106, doi: [10.1088/0004-637X/765/2/106](https://doi.org/10.1088/0004-637X/765/2/106)
- . 2013b, *ApJ*, 765, 106, doi: [10.1088/0004-637X/765/2/106](https://doi.org/10.1088/0004-637X/765/2/106)
- Zuo, W., Wu, X.-B., Liu, Y.-Q., & Jiao, C.-L. 2012, *ApJ*, 758, 104, doi: [10.1088/0004-637X/758/2/104](https://doi.org/10.1088/0004-637X/758/2/104)